Powder Diffraction 12

12.1 Introduction

The powder method was devised by Hull soon after the discovery of X-ray diffraction, and developed in detail by Hull [1] and by Debye and Scherrer [2]. Since that time, X-ray diffraction from powdered specimens has been used in divers investigations of materials. The main interest in this book is structure determination for which powder methods have, until recent years, been inappropriate, mainly because of the problem of overlap of the X-ray reflections which causes three-dimensional data information to collapse on to a one-dimensional powder record. The vast improvement in instrument technology in recent years has led to powder photographs and diffractograms of sufficient precision to be interpretable in terms of the underlying crystal structures, and powder techniques have now been developed as a very significant tool in X-ray structure determination. Before launching into this topic, however, we summarize here some of the many applications of X-ray powder diffraction other than in crystal structure determination.

12.1.1 Identification

An X-ray powder diffraction data file was inaugurated by Hanawalt in 1930, and his work has developed into the powder index of today. Well over a half a million substances have been indexed and recorded, and are represented by the Powder Diffraction File (PDF) of the International Centre for Diffraction Data (ICDD) [3], formerly the Joint Committee for Powder Diffraction Studies, which maintains a database of powder diffraction patterns, including inter alia the d-spacings and relative intensities of observable data.

12.1.2 Crystallinity: Size and Strain Broadening

Crystals produce sharp X-ray diffraction peaks, whereas amorphous materials, such as glass, liquids, and some polymers, produce a few diffraction maxima and a diffuse background. A decrease in crystallite size in a crystal sample causes an increase in the width of diffraction maxima, often characterized by the peak full width at half maximum height (FWHM), β, which is related to the mean crystallite size l by $\beta = K\lambda/(l\cos\theta)$, where the scale factor K is 0.89 for spherical crystallites, 0.94

M. Ladd and R. Palmer, *Structure Determination by X-ray Crystallography: Analysis by X-rays and Neutrons*, DOI 10.1007/978-1-4614-3954-7_12,

for cubic grains and otherwise generally close to unity. Powder methods can be used to determine the degree of crystallinity by comparing the intensity of the background pattern to that of the sharp peaks.

Most real crystals contain imperfections which produce distortions in the microstructure. Both decrease in crystallite size and increase of strain in a crystal will cause broadening of the recorded diffraction peaks. The Williamson-Hall analysis [4] allows both size and strain to be determined through the expression $\beta_{hkl} = 2\varepsilon d^*_{hkl} + 1/l$, where β and l are as before and ε is the microstrain. A plot of β against $1/l$ leads to values for both the crystallite size and the microstrain.

12.1.3 Unit-Cell Parameters

Powder diffraction data can be indexed and unit-cell parameters determined readily for cubic, hexagonal, and tetragonal crystals. Other crystal systems present more difficulty and we address this matter in Sect. 12.5, where we shall see that the most important factor is the precision obtainable in the measurement of 2θ from the diffraction data.

12.1.4 Expansion Properties

The unit-cell parameters depend on temperature and pressure. Changes in the d-spacings with changes in temperature or pressure allow the thermal expansivity and bulk modulus to be determined. As with the unit-cell parameters, measurements of 2θ are required. The bulk modulus K is given by the expression $K = -V(\partial p/\partial V)_{\mathrm{T}}$, and accurate unit-cell parameters are required to determine the volume change under uniform compression.

12.1.5 Phase Transitions and Alloy Systems

At certain critical conditions of temperature and pressure, a crystal may change its structure to a polymorphic form, and this is revealed by the appearance of new peaks in the diffraction record and the disappearance of some exhibited previously. Allied to this property is the study of alloy systems. Figure 12.1 shows an early powder pattern of the binary silver-cadmium alloy system [5], and Fig. 12.2 is the phase diagram [7] deduced from that study.

12.2 Crystal Structure Analysis with Powders

In recent years, great progress has been made in the determination of crystal structures from powder data, and these developments in the powder method have added a new and powerful tool for the determination of the structures of the many substances that could be obtained *only* in microcrystalline form, of particle size ca. 10^{-3} mm. This topic forms the subject matter for the rest of this chapter; more detailed discussions of powder methods can be found in the literature [8–11].

12.2.1 Crystal Structure Determination Scheme

A scheme for the structure determination of a crystal from powder diffraction data may be set out in five stages:

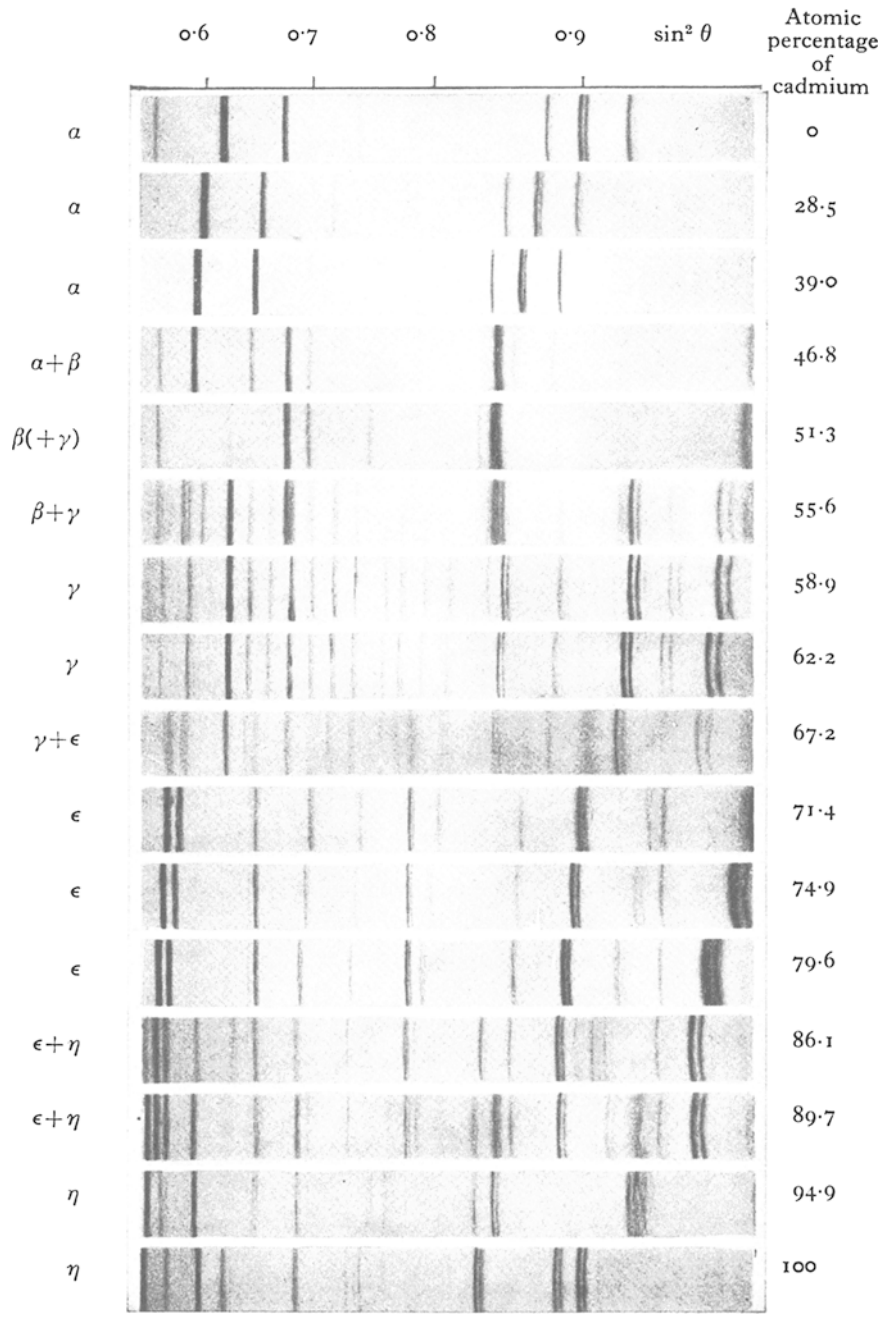

Fig. 12.1 Early X-ray powder photographs of silver–cadmium alloys, taken with Fe $K\alpha$ X-radiation. Silver, the α-phase, takes up cadmium into solid solution to the extent of ca. 40 % Cd. The unit-cell side a of the cubic α-phase is proportional to the concentration c_{Cd} of cadmium (Vegard's law [6]). Since the metallic radius of cadmium (1.50 Å) is greater than that of silver (1.44 Å), lines in the α-phase move to lower θ as c_{Cd} increases. Several films show $\alpha_1\alpha_2$ splitting at high θ (after Westgren and Phragmén, loc. cit. [4])

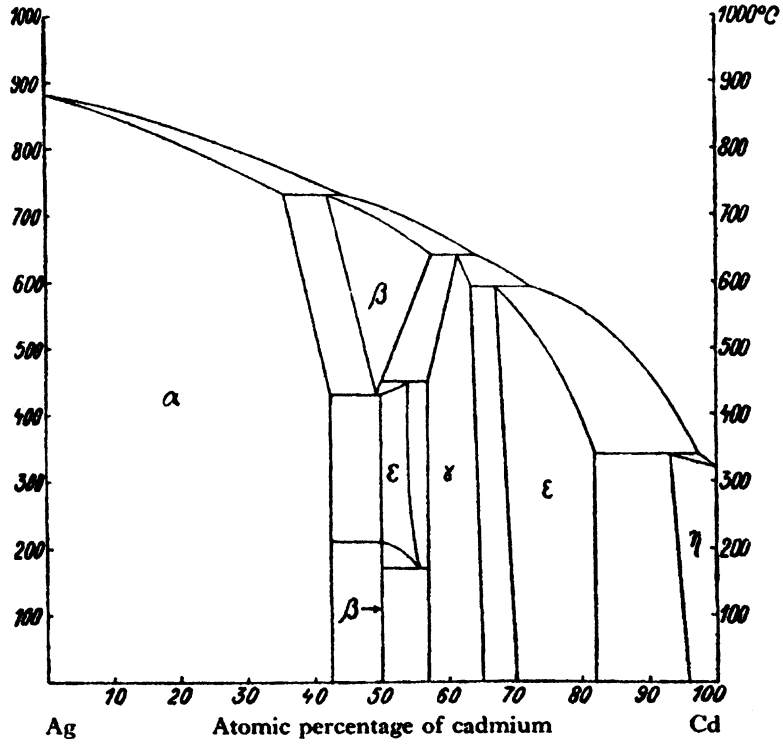

Fig. 12.2 The phase equilibrium diagram for the silver–cadmium system [5]; silver and cadmium form a continuous range of solid solutions, up to 42.5% Cd; the range at the high cadmium end is much smaller (reproduced by courtesy of John Wiley and Sons)

1. Collecting and indexing the powder diffraction pattern, and determining the unit cell
2. Identifying the space group from the diffraction record, if possible
3. Decomposing the powder pattern into integrated intensity data, $I(hkl)$
4. Solving the phase problem
5. Refining the model structure

As with single-crystal X-ray analysis, the first three stages lead to the acquisition of a set of relative $F_o(hkl)$ data; the indexed data will enable the space group to be determined as far as possible. The phase problem may be tackled by traditional Patterson or direct methods, or with direct-space techniques such as Monte Carlo or genetic algorithms, which make use of the power of modern computers. The refinement of the structure follows the Rietveld technique, developed in the late 1960s, which has been the driving force for the extension of the powder method to the more complex materials now studied.

The experimental data collection procedures have progressed greatly since the initial film based camera techniques, leading to refined camera methods and then to diffractometer methods, and with neutron and synchrotron sources as well as X-rays.

12.3 Basis of the Powder Method

The geometrical basis of X-ray powder photography is illustrated in Fig. 12.3. In the camera method, monochromatic, collimated X-rays enter along a diameter of the cylindrical camera, through a small hole in the X-ray film, and exit through a diametrically opposed aperture into a beam trap. In this type

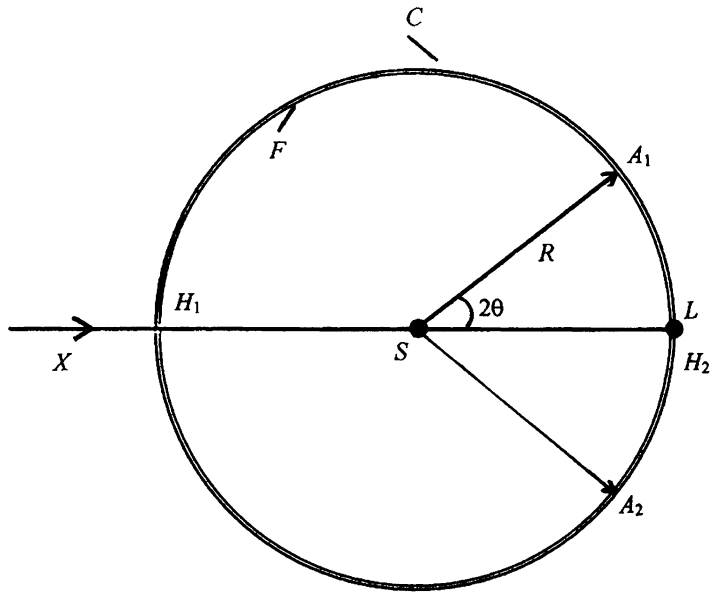

Fig. 12.3 The basic Debye–Scherrer arrangement for X-ray diffraction from polycrystalline specimens: C, camera housing of radius R, with film strip F fitted tightly against its inner surface; X, incident X-ray beam traveling along a diameter of the camera; H_1 and H_2, two small, diametrically opposed holes in the camera and film; S, the powder specimen; L, trap for the transmitted X-ray beam; A_1 and A_2, positions of two arcs of one and the same powder reflection; 2θ, the angle of scatter (twice the Bragg angle)

of camera, the specimen is a very finely ground powder contained in a thin-walled borosilicate glass capillary tube, so providing a cylindrical-shaped specimen. The mounting for the sample tube is provided with mechanical slides, so that it can be adjusted to rotate on its axis within its own volume. The rotation serves to increase the effective randomness of the orientations of the crystallites in the sample, but is not a necessary feature of the method itself. Other experimental techniques may require a specimen in the form of a flat plate.

Typical reflection positions on a powder film are shown at A_1 and A_2, at a scattering angle of 2θ. From the geometry of the camera, it is clear that θ is obtained from

$$\text{arc } A_1A_2 = 4R\theta \tag{12.1}$$

where R is the radius of the film. Since the crystallites lie in all possible orientations, the Bragg equation for a given reflection hkl is satisfied by any generator of a cone of semi-vertical angle $2\theta_{hkl}$ and axis along the transmitted X-ray beam. A complete cone of diffraction spots intercepts the cylindrical film strip in circular arcs, A_1 and A_2, of uniform intensity. If all possible orientations do not exist, as when the crystallites are too large, the arcs are broken to give a "spotty" powder photograph.

When the Bragg equation is satisfied for a reflection to occur, we have

$$\sin^2\theta = \lambda^2/(4d^2) \tag{12.2}$$

so that d values are also obtainable. An important limitation of the powder method is immediately evident, namely, that we can measure only one geometrical parameter, the Bragg angle θ for each reflection.

For a structure analysis, we know that we must obtain the unit-cell dimensions, the space group, and the *hkl* indices for each reflection together with its integrated intensity. Until the development of both high speed computing and improvements in the data collection procedures, the task was formidable, although some simplification arises for high-symmetry materials.

12.4 Data Collection

In powder diffraction work, many fewer resolved reflections are available than with single-crystal X-ray crystallography. In addition, the problem of determining the unit-cell dimensions, space group, and indices and intensities of reflections is less straightforward.

Powdered specimens contain numerous very small crystallites arranged in completely random orientations, so that there is no explicit information on the location of a reciprocal lattice point other than its distance d^* from the origin. A powder pattern is a collapsed, tangential projection of the weighted reciprocal lattice, in which each diffraction maximum is characterized by its Bragg angle θ and its intensity.

Powder lines have a significant breadth and tend to merge or overlap with both increasing θ and increasing unit-cell size. A sample containing crystallites that are too large may be ground in an appropriate apparatus, made from agate or tungsten carbide. Care must be exercised because over-grinding could introduce strain with consequent line broadening

In order that powder lines should be sufficiently well resolved for their positions to be measured to better than the desired 0.01° in θ, it is necessary that the X-radiation is monochromatic, very finely focused on to the film, and produces a low intensity of background radiation.

12.4.1 Guinier-Type Cameras

One method of obtaining the desired experimental conditions is with a Guinier-type camera, employing a curved crystal monochromator. This X-ray monochromator consists essentially of an asymmetrically ground, curved crystal of quartz, silicon, or germanium. The $(10\bar{1}0)$ planes of a quartz crystal, or the (111) planes of silicon or germanium, are set to diffract at a prearranged angle to the crystal surface, Fig. 12.4a. The crystal is ground to a cylinder of radius $2R$ and then bent over the fitting area. X-rays from the line focus of the X-ray tube strike the crystal as a divergent bundle. In the crystal, a narrow wave band is separated from the polychromatic source by diffraction according to the Bragg equation. The diffracted rays leave the crystal as a convergent bundle, at the glancing angle θ. The most intense spectral line is the $K\alpha_1$, and the crystal is set to reflect this wavelength, with the elimination of other wavelengths from the diffracted beam, albeit with a slight loss in the α_1 intensity.

Figure 12.4b shows the location of the various determinants involved in the setting of the crystal monochromator. The distance a between the line focus F of the X-ray tube and the center of the crystal, and the distance b between the center of the crystal and the focal line F' are maintained constant for different wavelengths by a judicious choice of τ, the angle between the $(10\bar{1}0)$ or (111) planes and the crystal surface. This feature allows a change of X-ray tube (and wavelength) without major alterations in the experimental arrangement.

The principle of Guinier operation is illustrated in Fig. 12.4c. The Guinier-type camera can function in transmission geometry, as with low–medium absorbing specimens, or in reflection geometry, in the case of strongly absorbing materials. In the photographic technique, the X-ray film is mounted on the Seeman–Bohlin focusing cylinder. Figure 12.5 shows a complete Guinier-type

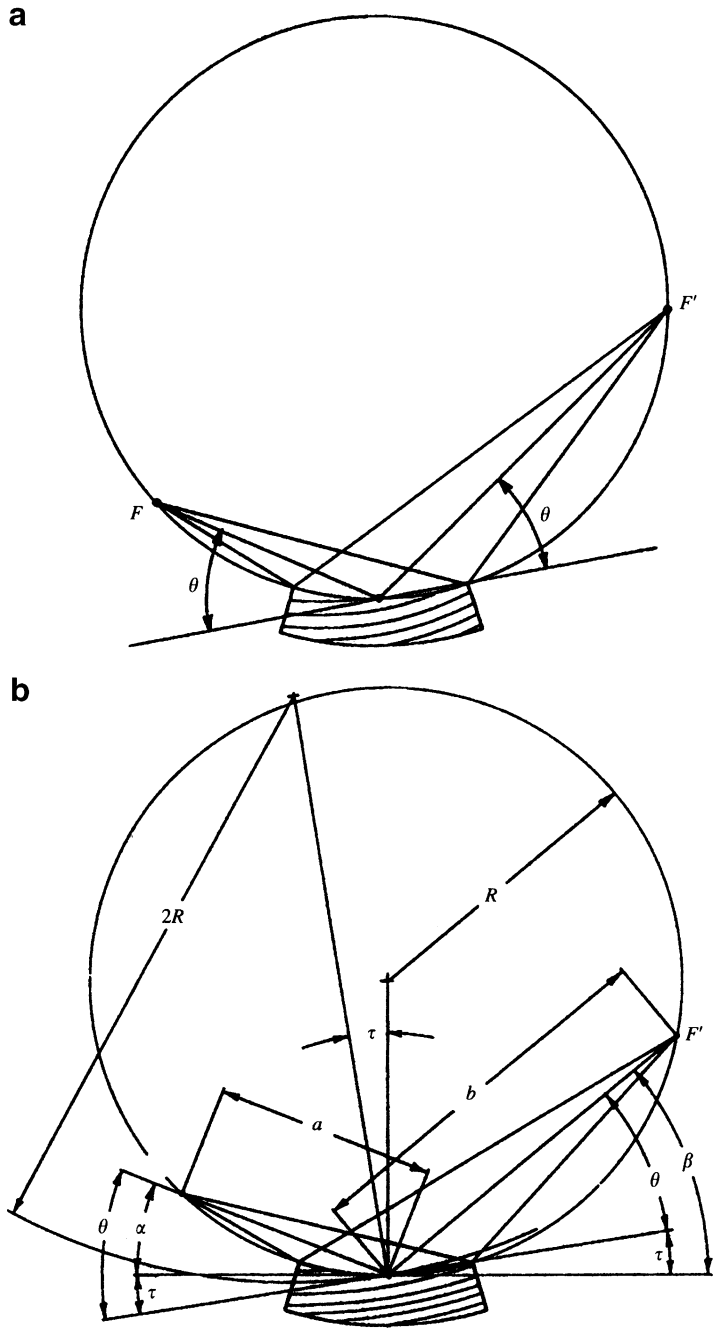

Fig. 12.4 (**a**) A curved crystal monochromator, showing the incident divergent bundle of rays from the X-ray tube at F reflected at the glancing angle θ, and the bundle convergent at the point F'. (**b**) The curved crystal, showing the determinants involved in the setting of the crystal; the constancy of a and b with change of wavelength depends on the correct choice of τ. (**c**) The principle of the Guinier method, showing the disposition of X-ray tube, monochromator, powder specimen, and focusing cylinder. The focusing cylinder carries a photographic film, or can be replaced by a scintillation counter (diffractometer) or an imaging plate (imaging camera) (courtesy Huber Diffraktionstechnik GmbH, 83253 Rimsting, Germany)

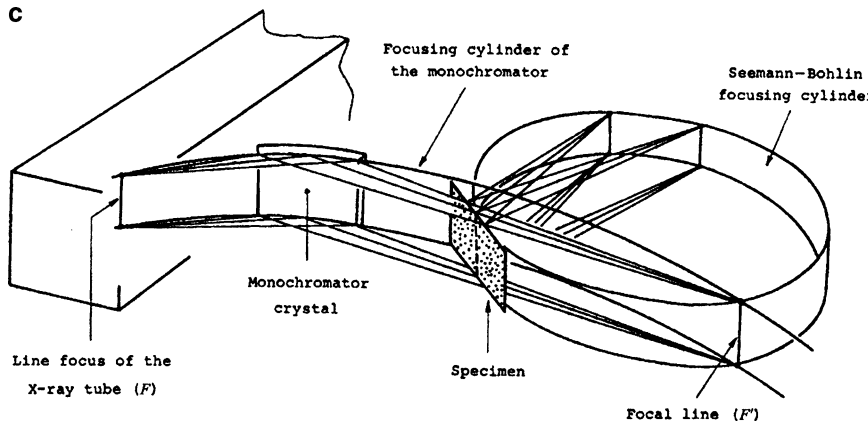

Fig. 12.4 (continued)

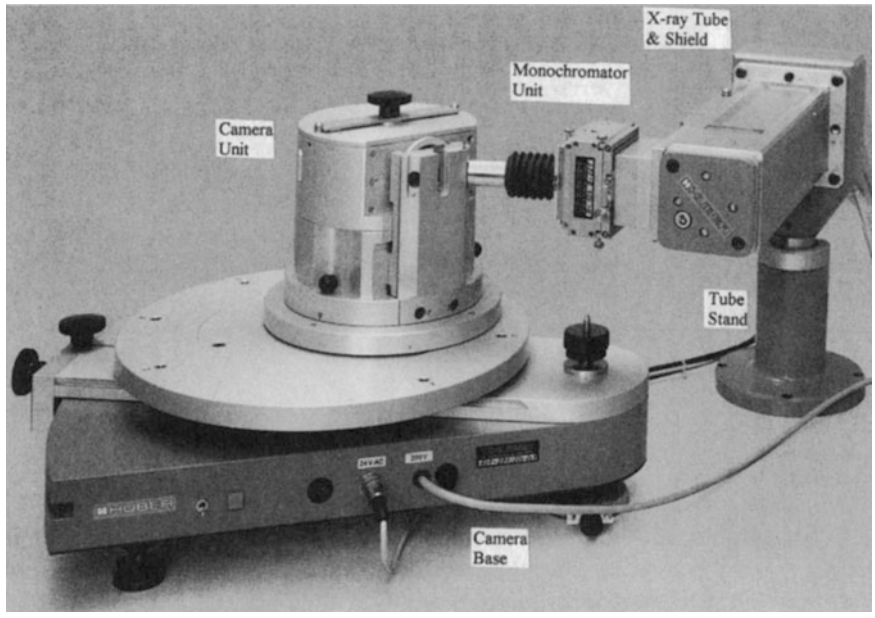

Fig. 12.5 Huber–Guinier Powder Camera assembly (courtesy Huber Diffraktionstechnik GmbH, 83253 Rimsting, Germany)

film-camera assembly for flat, powdered specimens. If the final film is assessed with a vernier measuring instrument, the desired accuracy in θ can be achieved.

12.4.2 Image Plate Camera

In a modern development of the Guinier technique, the X-ray film is replaced by an image (photo-stimulated) plate, leading to greatly improved speed of data collection without loss of the accuracy that is so important in powder indexing. The X-ray imaging plate is a flexible strip, like an X-ray film,

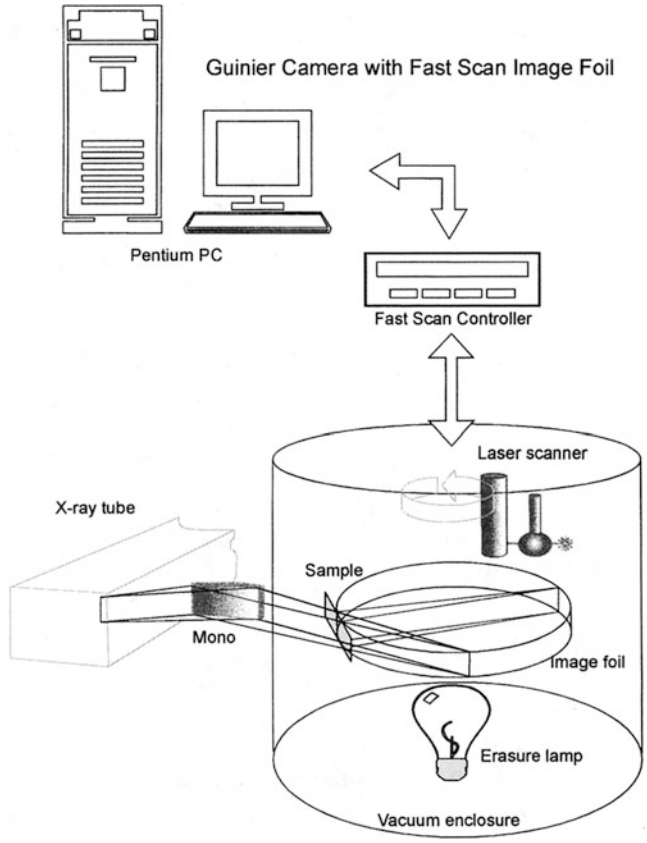

Fig. 12.6 Schematic diagram of the Huber Imaging Powder Camera. The powder pattern, collected on the imaging plate, is scanned by a laser and then digitized for computer analysis (courtesy Huber Diffraktionstechnik GmbH, 83253 Rimsting, Germany)

that contains a metastable phosphor, such as a deposited 150 μm layer of BaFBr.Eu(II) which contains F-centers (color centers) in an organic binder, as discussed in Sect. 5.7.3.

The advantages of the imaging plate are parallel data collection over a large area, with high dynamic range, good resolution, and digital readout. The image-recorded intensity tends to decay with time, so that the plates are best handled in darkened conditions.

Figure 12.6 is a schematic diagram of the Huber Imaging-Plate Guinier camera. The incident beam is monochromatic $K\alpha_1$ X-radiation, focused on to powder specimen in a flat holder. The camera enclosure may be evacuated, so as to decrease the background scattering. The imaging plate containing the powder pattern is scanned by a laser, and software handles the scanned data to produce a profile record and data files. Collection times may be reckoned in minutes, particularly where a synchrotron source is available. After use, the imaging plate is restored to its original condition by means of the halogen erasure lamp. The data files are produced in a format appropriate for Rietveld refinement (q.v.). Fuller details of the performance of the camera are available from the manufacturer [12].

12.4.3 Powder Diffractometers

The diffractometer is the primary instrument for recording powder diffraction spectra, whether produced by X-ray or neutron radiation sources. Many X-ray powder diffractometers use the Bragg-Brentano

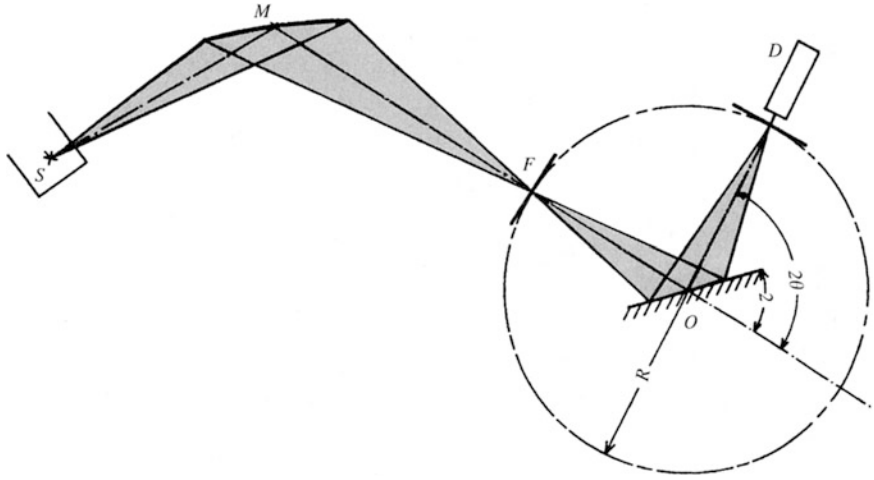

Fig. 12.7 Schematic diagram of a powder diffractometer with Bragg-Brentano parafocusing: *S*, X-ray source focus; *M*, curved-crystal monochromator; *F*, adjustable receiving slit; *O*, rotation axis; *D* detector; *R*, radius of focusing circle (after Huber Diffraktionstechnik GmbH, 83253 Rimsting, Germany)

parafocusing principle in reflection geometry, Fig. 12.7. The take-off angle of X-rays from the tube anode is about 6°, impinging as a divergent beam at the monochromator. In a high-resolution experimental arrangement, the pre-sample crystal monochromator, of the type in Fig. 12.4b, removes the unwanted $K\alpha_2$ radiation, since the path of this radiation from the monochromator deviates from that of the $K\alpha_1$. The reflected X-rays converge at a knife-edge slit and then diverge on to the specimen. Scattered X-rays from the flat sample converge at a receiving slit and are received at the proportional counter, gas or solid state device, detector assembly. The detector rotates about the sample axis synchronously through twice the angular rotation of the sample in the $\theta/2\theta$ scan mode. The effective source, receiving slit and sample lie on the focusing circle, which has a radius that depends on θ. It is important to avoid preferred orientation in the flat plate powder sample when preparing it for diffractometer [13]. The sample is spun about an axis normal to the plate so as to obtain a good average diffraction record. It is also desirable to move the capillary tube containing the powder sample such that a different part of it is irradiated as the data collection proceeds, so as to counteract the effects of any decomposition of the sample. Figure 12.8 illustrates a typical high-resolution powder diffractometer assembly.

Synchrotron Radiation

The use of synchrotron radiation instead of X-rays leads to better resolution, but in view of the cost of SR facilities, it is necessary to carry out a preliminary X-ray examination, as with single crystals, so as to obtain the unit-cell data and to index the pattern. Particular advantages of synchrotron radiation are the high intensity and excellent vertical collimation, leading to greatly improved resolution compared with laboratory X-ray sources. These features decrease the difficulties caused by overlapping reflections, and have enabled structures of considerable complexity to be solved, such as that of the compound $La_3Ti_5Al_{15}O_{37}$, which has 60 atoms in the asymmetric unit [14].

12.4.4 Diffractometry at a Neutron Source

We have discussed features of neutron diffraction in detail in Chap. 11, and the technique is of importance in structural studies with powder specimens. The majority of neutron research projects are

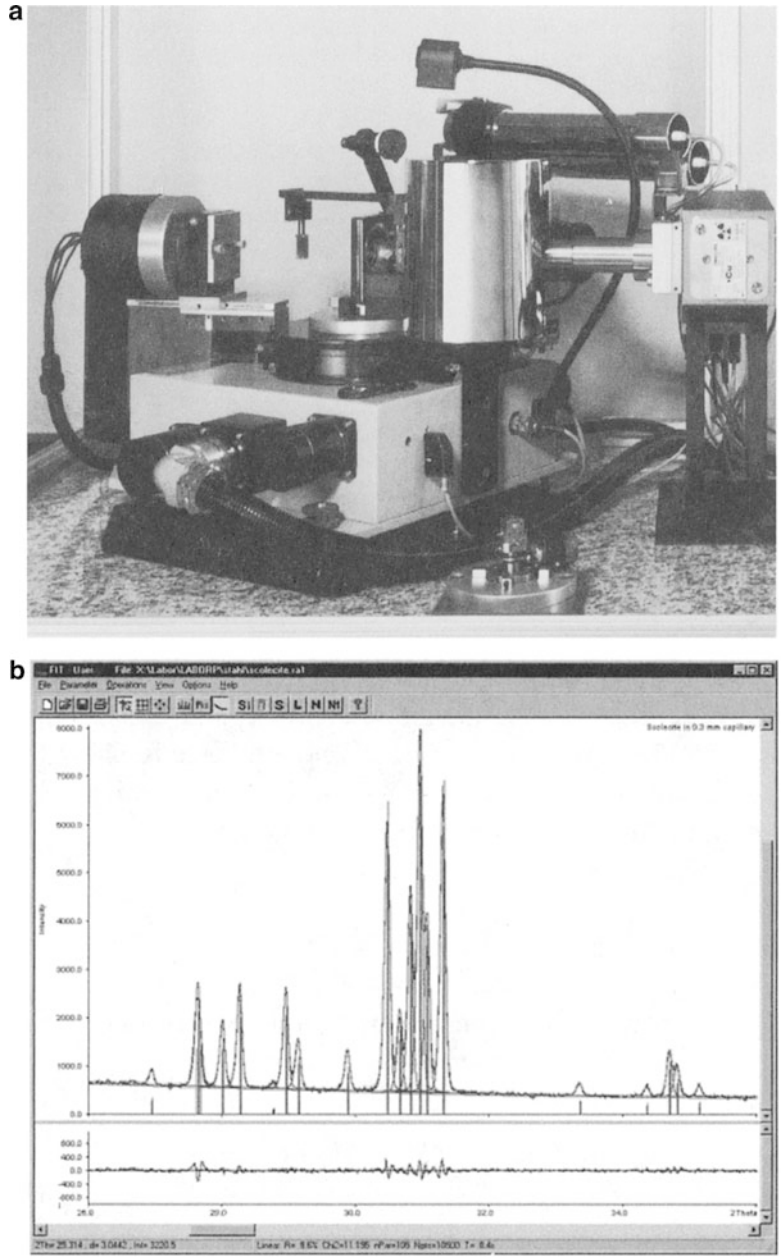

Fig. 12.8 (**a**) The Stoe STADI *P* powder diffractometer system: the radiation is $K\alpha_1$, in the range available from Fe to Mo targets; the focusing circle diameter is 130 mm, the 2θ range is 0–140°, and the minimum step size is 0.0005°. Intensities are measured by a scintillation counter, and the whole operation is handled by built-in structure-solving software. (**b**) A diffractogram of solecite, a calcium-containing zeolite, measured in the Debye–Scherrer transmission mode in a capillary of 0.3 mm diameter: calculated and experimental peaks (with probable errors indicated), positions of main peaks (*vertical lines*) and, below, the difference curve are shown (courtesy Stoe & Cie GmbH, Darmstadt, Germany)

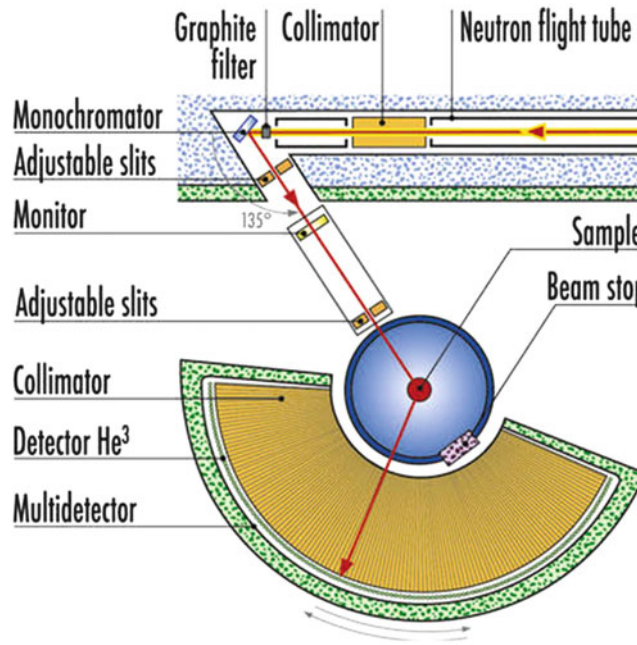

Fig. 12.9 Schematic diagram of the D2B very high-resolution, two-axis neutron powder diffractometer D2B at the Institut Laue-Langevin (reproduced from the "yellow book" by courtesy of the Institut Laue-Langevin, Grenoble)

carried out at the nuclear reactor at the Institut Laue-Langevin in Grenoble. The fission process used to produce a neutron flux generates much heat and has to be water-cooled, by D_2O. The deuterated water also slows the "thermal" neutrons to the ambient temperature, leading to a neutron source of wavelength of 1–2 Å.

Owing to the size of the neutron beam, the single crystal for the monochromator must be large. Typically, germanium crystals are cut so that the (*hhl*) planes, often the (220), are in a position to act as a monochromatic source. Filters may be incorporated in order to select a particular wavelength.

Neutrons are detected mainly by absorption in a gas (often helium) proportional counter. In the detection process, the (n, γ) reaction is

$$^3_2\mathrm{He} + ^1_0\mathrm{n} \rightarrow ^4_2\mathrm{He} + \gamma$$

and the energy of the γ-radiation is proportional to the intensity of the X-ray signal. The quantum efficiency Q of the detector is given by

$$Q = 1 - \exp(\sigma p l)$$

where σ is the neutron cross section, p is the pressure of the helium gas, and l is the length of the chamber of the proportional counter.

The resolution is high and the peak shape, though complicated, is well understood and can be modeled very satisfactorily in a refinement process. Because the neutron cross section, the neutron equivalent of the X-ray form factor, is almost constant over the whole range of $\sin\theta/\lambda$, atomic coordinates and temperature factors can be obtained with high precision. The method can be applied both at low temperatures and at high pressures. Figure 12.9 is a diagrammatic illustration of a high-resolution powder diffractometer at the Institut Laue-Langevin that uses a neutron source and a graphite filter. It was designed to achieve the ultimate resolution, $\Delta d/d = 5 \times 10^{-4}$, limited only by

particle size. Data can be collected on a 500 mg sample in a few hours and on a gram sample in a few minutes, with obvious advantages.

Crystal Structure of Benzene

The crystal structure of benzene at low temperature has been studied by this technique [15]. Notwithstanding its highly symmetrical molecular shape, benzene crystallizes in the orthorhombic system, with space group *Pbca*: $a = 7.3551(3)$ Å, $b = 9.3712(4)$ Å, $c = 6.6994(3)$ Å, and four molecules in the unit cell; the figures in parentheses are the estimated standard deviations of the unit-cell parameters.

The molecules lie in special positions of this space group so that the molecular symmetry that is indicated crystallographically is only $\bar{1}$. In practice, deuterated benzene was used because the incoherent scattering from hydrogen results in a very high background level; deuteration of hydrogen-containing materials is standard practice with neutron experiments. Furthermore, the neutron scattering length for deuterium is positive at 6.671 fm[1] whereas that for hydrogen is −3.739 fm.

The precision of the structure analysis can be judged from the following bond length parameters, quoted in Å:

$$\begin{aligned} C_1{-}C_2 &= 1.3969(7), \quad C_1{-}D_1 = 1.0879(9) \\ C_2{-}C_3 &= 1.3970(8), \quad C_1{-}D_1 = 1.0869(9) \\ C_3{-}C_1 &= 1.3976(7), \quad C_1{-}D_1 = 1.0843(8) \end{aligned}$$

The mean values for C–C and C–D are 1.3972(5) Å and 1.0864(7) Å, respectively. The differences between the individual C–C and C–D bond lengths are not significant at the 3σ level, so that there is no evidence to show that the geometry of benzene is other than truly hexagonal. For further discussions on neutron diffractometry, the reader is referred to the literature [16, 17].

Time-of-Flight Techniques

Time-of-flight (TOF) techniques use a polychromatic beam and a pulsed neutron source. From the de Broglie equation, it follows that the neutron wavelength is inversely proportional to its speed. By detecting the time of arrival of each neutron of a particular pulse, its wavelength and the corresponding d-spacing can be determined:

$$\lambda = h/m_n v = ht/m_n l = 2d \sin\theta$$

where l is the flight path length and t is the TOF. By differentiating the above expression, it follows that a long flight path and large scattering angle enable good resolution at small d values to be achieved. The TOF technique permits good use of the total neutron energy. Peak shapes are more complicated and consequently more difficult to model than those from monochromatic sources.

Time-Resolved Studies: MYTHEN Detector

The MYTHEN single-photon-counting silicon microstrip detector has been developed at the Swiss Light Source of the Paul Scherrer Institute, Switzerland [18] for time-resolved powder diffraction experiments. In these experiments, a reaction is triggered rapidly and synchrotron X-rays used to probe the structural changes as a function of time. This technique has application, for example, in the study of

[1] fm = femtometer, 10^{-15} m.

how protein molecules behave under protein action. The procedure needs sub-second time resolution, and the Laue stationary crystal method is used.

The MYTHEN detector [19] allows the acquisition of diffraction patterns over 120° in 2θ in fractions of seconds. The quality of the data obtainable is comparable with that of normal high-resolution detectors in terms of FWHM resolution and in profile shape. It has the additional advantage of fast and simultaneous acquisition of the full diffraction pattern. MYTHEN is therefore highly desirable for time-resolved studies, such as radiation damage in organic compounds [20].

12.5 Indexing Powder Patterns

The simplest powder diffraction pattern is obtained for cubic crystals. In the cubic system, (12.2) may be written as

$$\sin^2\theta = \frac{\lambda^2}{4a^2}(h^2 + k^2 + l^2) = \frac{\lambda^2}{4a^2}N_c \tag{12.3}$$

where N_c is the integer sum $(h^2 + k^2 + l^2)$. It follows that the values of $\sin^2\theta$ must exhibit integer ratios with cubic crystals, within the limits of experimental error, and that the integer N_c follows one of the three clearly defined possible patterns: 1,2,3,4,... for a P unit cell; 2,4,6,8,... for I; and 3,4,8,11,... for F, according to the known limiting conditions for X-ray reflections. Hence, the indexing of a cubic substance is normally a simple matter. But even with this high symmetry, more than one reflection can have the same value of θ. For example, pairs such as 300 and 221 ($N_c = 9$), and 411 and 330 ($N_c = 18$) are superimposed on the X-ray film. Certain values of N_c, such as 7, 15, 23, 28, 31,..., in general, $m^2(n - 1)$ values, where m and n are integers, cannot arise in the cubic system because they cannot be derived as the sum of the squares of three integers. Although the unit cell can be identified readily, we see that there is already a problem in assigning the correct relative intensities to these superimposed reflections.

We referred to an apparent P unit cell for potassium chloride in Sect. 2.10.1. It is, perhaps, interesting here to note that Fig. 12.10 shows indexed powder photographs of sodium and potassium

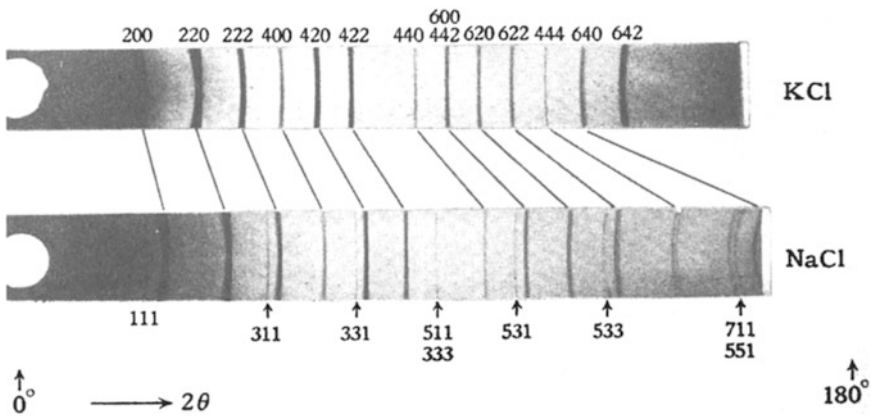

Fig. 12.10 Indexed X-ray powder photographs for KCl and NaCl. Both structures have the space group $Fm\bar{3}m$, but the apparent absence of powder lines with h, k, and l all odd in KCl causes it to appear as $Pm\bar{3}m$ with a spacing $a_{\text{apparent}} = a_{\text{true}}/2$ (after Bragg, *The Crystalline State*, vol 1, [94])

chlorides. Although both potassium chloride and sodium chloride have the same structure type, the absences in the pattern for potassium chloride caused it to be considered as primitive cubic at first. The reflections for which h, k, and l are all odd integers are accidental absences, that is, reflections too weak to be recorded; see Sect. 4.2.3.

Powder patterns may be indexed by trial and error methods for simple crystal structures of the cubic, tetragonal, and hexagonal systems, by use of equations like (12.3), but as the crystal structure becomes complex, with lower symmetry and larger unit-cell dimensions, the problem is enhanced: the powder lines become very close, merging into and overlapping one another, so that indexing and intensity measurement become increasingly difficult.

12.5.1 General Indexing

The indexing of powder diffraction patterns is carried out today by computer programs, and success in this process depends to some extent on the complexity of the structure, and to a very large extent on the accuracy of the primary θ-data. An early general procedure for indexing was set out by Ito [21].

We recall the general equation for $d^*(hkl)$, developed in Sect. 2.4:

$$d^{*2}(hkl) = h^2a^{*2} + k^2b^{*2} + l^2c^{*2} + 2klb^*c^* \cos\alpha^* + 2lhc^*a^* \cos\beta^* + 2hka^*b^* \cos\gamma^* \tag{12.4}$$

Generally, this equation is cast in terms of Q values, for convenience, such that $Q_{hkl} = d^{*2}(hkl)$, $Q_A = a^{*2}, \ldots, Q_D = 2b^*c^* \cos\ \alpha^*, \ldots$, and so on, so that

$$Q_{hkl} = h^2Q_A + k^2Q_B + l^2Q_C + klQ_D + lhQ_E + hkQ_F \tag{12.5}$$

It follows that

$$Q_{hkl} = 4\frac{\sin^2\theta(hkl)}{\lambda^2} \tag{12.6}$$

Magnesium Tungstate

As an example, Table 12.1 lists a set of 40 Q values for magnesium tungstate, $MgWO_4$ collected by a film technique. Any three noncoplanar reciprocal lattice vectors define a possible unit cell. A unit cell thus chosen may not be the smallest, conventional unit cell, but if it is a satisfactory cell it may subsequently be transformed as we discuss shortly. We will consider Ito's method by means of this hand-solved example.

Normally, there will be no a priori knowledge of three suitable noncoplanar vectors. Hence, we consider the first three lines in the diffraction pattern, and label them initially as Q_{100}, Q_{010}, and Q_{001}, so that here we have $a^* = 0.1761$ Å, $b^* = 0.2131$ Å, and $c^* = 0.2683$ Å. We look through the pattern for multiples of these values, so as to improve the values of the reciprocal parameters by averaging the results. For example, $Q_{200} = 4Q_{100} = 0.1240$, and line number 7 at $Q = 0.1239$ is evidently Q_{200}, within experimental error. Proceeding in this way as far as possible, we obtain the average values $a^* = 0.1761$ Å, $b^* = 0.2131$ Å, and $c^* = 0.2684$ Å.

Next, we consider a zone in which one index is zero, say, $hk0$. If the angle γ^* is not 90°, we would expect to find two lines symmetrically disposed about the position that would correspond to Q_{110} if γ^* was 90°. For example, assuming correctness so far, $Q_{100} + Q_{010} = 0.0764$. In the list of Q values, we

Table 12.1 Values of Q from the powder diffraction pattern of magnesium tungstate

Line number	Q	Line number	Q
1	0.0310	21	0.3246
2	0.0454	22	0.3322
3	0.0720	23	0.3364
4	0.0764	24	0.3418
5	0.1164	25	0.3451
6	0.1186	26	0.3505
7	0.1239	27	0.3646
8	0.1649	28	0.3723
9	0.1695	29	0.3824
10	0.1816	30	0.4016
11	0.1957	31	0.4083
12	0.2077	32	0.4432
13	0.2123	33	0.4465
14	0.2386	34	0.4500
15	0.2436	35	0.4608
16	0.2517	36	0.4659
17	0.2563	37	0.4770
18	0.2793	38	0.4863
19	0.2884	39	0.4918
20	0.3055	40	0.4960

Table 12.2 Some calculated and observed Q_{hk0} values for magnesium tungstate

$hk0$	Q_{calc}	Q_{obs}
110	0.0764	0.0764
210	0.1694	0.1695
310	0.3244	0.3246
120	0.2126	0.2123
220	0.3056	0.3055

have line 4 at 0.0764, and no pair of lines exists symmetrically disposed about this position, as there would be if γ^* was not 90°. Thus, we conclude that line 4 is 110, and that $\gamma^* = 90°$.

We expect now to find other Q_{hk0} values among those listed in Table 12.1. For example, $Q_{210} = 4Q_A + Q_B = 0.1694$, so that the line at 0.1695 corresponds to Q_{210} in the given data. A few $hk0$ lines are listed in Table 12.2, showing that we are on the right lines.

In a similar manner, $Q_{010} + Q_{001} = 0.1174$. There is no line of this Q value, but lines 5 and 6 are nearly symmetrically disposed about this position, so that these lines may be taken as $0\bar{1}1$ and 011. Since $Q_{011} - Q_{0\bar{1}1} = 4b^*c^* \cos\ \alpha^*$, it follows that $\alpha^* = 89.45°$. As before, we can now check for the presence of Q_{0kl} values, as desired. For example, $Q_{021} = 4Q_{020} + Q_{001} + 2Q_D(4b^*c^* \cos\alpha^*) = 0.2558$; similarly, $Q_{02\bar{1}} = 0.2514$. These Q values correspond to lines 17 and 16.

We seek β^* in a similar manner. By trial and error in this way, it is found ultimately that lines 11 and 32 are nearly symmetrically disposed about the calculated value, 0.3190, of Q_{102}. Hence, β^* evaluates to 49.11°. Summarizing the results, we have the reciprocal unit cell

$$a^* = 0.1761\,\text{Å}, \quad b^* = 0.2131\,\text{Å}, \quad c^* = 0.2684\,\text{Å}$$
$$\alpha^* = 89.45°, \quad \beta^* = 49.11°, \quad \gamma^* = 90.00°$$

Table 12.3 Indices and Q values for magnesium tungstate

Line	hkl	Q_{calc}	Q_{obs}	Line	hkl	Q_{calc}	Q_{obs}
1	100	0.03101	0.0310	21	310	0.32444	0.3249
2	010	0.04541	0.0454	22	$41\bar{2}$	0.33250	0.3322
3	001	0.07203	0.0720	23	012	0.33568	0.3364
4	110	0.07644	0.0764	24	$22\bar{2}$	0.34197	0.3418
5	$01\bar{1}$	0.11637	0.1164	25	$32\bar{1}$	0.34491	0.3451
6	011	0.11851	0.1186	26	$3\bar{2}\bar{1}$	0.34937	0.3505
7	200	0.12403	0.1239	27	211	0.36626	0.3646
8	101	0.16491	0.1649	28	$12\bar{2}$	0.37272	0.3723
9	$2\bar{1}0$	0.16948	0.1695	29	$1\bar{2}\bar{2}$	0.38135	0.3824
10	020	0.18165	0.1816	30	$40\bar{3}$	0.40195	0.4016
11	$30\bar{2}$	0.19597	0.1957	31	030	0.40871	0.4083
12	$21\bar{2}$	0.20791	0.2077	32	$21\bar{3}$	0.44324	0.4432
13	$3\bar{1}\bar{1}$	0.21202	0.2123	33	$41\bar{3}$	0.44409	0.4465
14	$11\bar{2}$	0.23864	0.2386	34	$2\bar{1}\bar{3}$	0.44973	0.4500
15	$3\bar{1}\bar{2}$	0.24357	0.2436	35	320	0.46063	0.4608
16	$02\bar{1}$	0.25177	0.2517	36	$02\bar{2}$	0.46548	0.4659
17	021	0.25582	0.2563	37	$4\bar{2}\bar{2}$	0.47534	0.4770
18	300	0.27908	0.2793	38	$1\bar{1}2$	0.48616	0.4863
19	002	0.28812	0.2884	39	112	0.49041	0.4918
20	220	0.30562	0.3055	40	400	0.49614	0.4960

Finally, we obtain the direct space unit cell; Sects. 3.4 and 13.6.3—program RECIP, and then calculate the Q values, Sect. 13.6.9, so as to identify and index all lines in the diffraction record, as shown in Table 12.3. The results show good agreement between Q_{obs} and Q_{calc} for most of the lines, although certain fits suggest that some errors exist among the data. We see already in this fairly simple example the importance of the accurate experimental measurement of θ values.

12.5.2 Reduced and Conventional Unit Cells

From the results so far, the crystal system of magnesium tungstate appears to be triclinic. However, we must determine whether or not this unit cell is the conventional unit cell for the lattice, that is, it is correctly related to the lattice symmetry according to the conventions that we have discussed in earlier chapters. The real space unit cell is derived using the equations developed in Sect. 3.4, or with the program RECIP by entering the reciprocal unit-cell parameters, with the constant K equal to 1. Thus, we obtain

$$a = 7.512\,\text{Å}, \quad b = 4.693\,\text{Å}, \quad c = 4.929\,\text{Å}$$
$$\alpha = 90.72°, \quad \beta = 130.89°, \quad \gamma = 89.52°$$

or, in the usual order of increasing unit-cell lengths, as

$$a = 4.693\,\text{Å}, \quad b = 4.929\,\text{Å}, \quad c = 7.512\,\text{Å}$$
$$\alpha = 130.89°, \quad \beta = 89.52°, \quad \gamma = 90.72°$$

The order makes no difference to the reduced cell; it alters only the transformation matrix between the input and the reduced unit cells. A two-stage process now allows the determination of the reduced and conventional unit cells.

The unit-cell parameters derived from the indexing procedure are transformed to a unique, reduced unit cell based on the three shortest noncoplanar translations in the lattice—a Niggli-reduced cell [22, 23]; such a unit cell is always primitive. In the second stage, the distribution of twofold axes is determined, because it will define the lattice symmetry [24], Sect. 1.4.2 and Table 1.5. We know, for example, that the normal to a plane in a lattice that contains p intersecting twofold axes is itself a p-fold axis, and that a mirror plane exists normal to a p-fold axis ($p = 2, 4, 6$) in a lattice.

The two-stage procedure, which is lengthy manually, has been brought together in the program LEPAGE [25]. We describe this program further in Sect. 13.6.10, but for the moment we use it with the unit cell derived from indexing the $MgWO_4$ diffraction pattern. Thus, we obtain

	a (Å)	b (Å)	c (Å)	α (°)	β (°)	γ (°)
Input cell P	4.693	4.929	5.712	130.89	89.52	90.72
Reduced cell P	4.693	4.930	5.679	90.12	90.01	90.72
Conventional cell P	4.693	4.929	5.679	90.12	90.01	90.72

We see that the reduced and conventional unit cells are identical in this example. Further interpretation now depends upon the error permitted in the collinearity of the twofold axes in the real and reciprocal unit cells, the "2-axis criterion (in the program)." Ideally, it should be zero. However, there will be experimental errors in the data that are conveyed to the parameters; if we dismiss these errors, we may fail to recognize the true symmetry. In the present case, if all angles are regarded as 90° within experimental error, the lattice is P orthorhombic, with a 2-axis criterion of 1°. A more realistic situation could be to set α and β at 90°; then we obtain monoclinic P, under the more stringent 2-axis criterion of 0.5°:

$$\begin{aligned} a &= 4.693\ \text{Å}, & b &= 5.679\ \text{Å}, & c &= 4.929\ \text{Å} \\ \alpha &= 90(89.88)^\circ, & \beta &= 90.72^\circ, & \gamma &= 90^\circ \end{aligned}$$

where the unit cell has been rearranged so that the unique angle is β. Notice that this result would have been obtained immediately from the first reduction by imposing monoclinic symmetry. Some of the difficulty in this indexing analysis for magnesium tungstate arose from the fact that the data was not of the highest quality. The modern camera and, particularly, the diffractometer techniques described above ensure data of a sufficiently high quality.

12.5.3 Computer Indexing of the Diffraction Pattern

We have shown that determining the unit cell by hand can be a slow process, and it is not surprising to find that the literature today abounds with computer programs for indexing a powder pattern. Most of these programs that serve to determine the unit cell are stand-alone programs, but a few are part of a structure-solving and refinement package that leads to a complete structure determination, just like the single-crystal methods that we have described already.

Indexing a powder pattern, by whatever method, is an inductive process: we must deduce the indices of the diffraction lines from the experimental Q values. The first 20–30 lines in a pattern, starting from the low-θ region, are most important in indexing, because Q_{calc} involves the square of the indices, and so errors in Q_{obs} become more important as θ increases. We examine first the ITO (named after T. Ito, who devised the general method) program system.

ITO Program System

The program ITO12 is the 12th version of this program system [26]; a later version is now available, Sect. 13.7, but it is only very slightly different from version 12; see also Appendix D. It is a deductive program based on the properties of crystal zones, that is, planes of reciprocal lattice points passing through the origin, and is often described as *zone-indexing*. It performs best when given 30–40 accurately measured powder lines.

Any zone is specified by three parameters; for example, the zone $hk0$ may be formulated by

$$Q_{hk0} = h^2 Q_A + k^2 Q_B + hk Q_F \tag{12.7}$$

Two Q values are selected and assigned as Q_{100} and Q_{010}, similar to the procedure in Sect. 12.3. Expanding (12.7), we have

$$Q_{hk0} = h^2 Q_{100} + k^2 Q_{010} + 2hk(Q_{100}Q_{010})^{1/2} \cos\ \gamma^* \tag{12.8}$$

Let

$$\begin{aligned} 2hk(Q_{100}Q_{010})^{1/2} \cos\gamma^* &= R \\ &= \frac{Q_{hk0} - h^2 Q_{100} - k^2 Q_{010}}{hk} \end{aligned} \tag{12.9}$$

Values for Q_{hk0} are obtained from the experimental data, and used in the right-hand term of (12.9) so as to obtain a list of $|R|$ values. Agreements in $|R|$, within a permitted error, are then used to find a value for the angle γ^*. Zones that are found are checked and reduced, and the three zone parameters refined by least squares. Zone quality is determined by a parameter $1/P$, where P is the probability that a zone is found by chance. Pairs of zones with a common row are sought and the angle between them calculated. The unit cells found are reduced and transformed to standard form, and the first 20 lines indexed where possible. The fit is assessed by the M_{20} parameter:

$$M_{20} = \frac{Q_{20}}{2\bar{Q}N_{20}} \tag{12.10}$$

where Q_{20} is the Q value for the 20th indexed line, $\bar{Q}$ is the average error between Q_{obs} and Q_{calc} for the first 20 lines, and N_{20} is the number of lines, observed and calculated, up to Q_{20}. The program is optimized for the lower symmetry systems, orthorhombic, monoclinic, and triclinic. High-symmetry lattices may be reported in an orthorhombic setting, with a note that a higher symmetry lattice may exist.

Notes on the practical use of the program ITO appear in Sect. 13.7, and problems on it are given at the end of this chapter. The data for magnesium tungstate, Sect. 12.5.1, when used with ITO12, led to the unit-cell dimensions $a = 4.929$ Å, $b = 5.678$ Å, $c = 4.693$ Å, $\alpha = 90°$, $\beta = 90.77°$, and $\gamma = 90°$, in good agreement with the values derived in the worked example of this substance.

CRYSFIRE Program System

The program system CRYSFIRE provides a detailed set of procedures for indexing powder patterns. In common with all methods, a prerequisite is a set of Q values with errors less than ca. $0.01°$ in θ. As we have seen, this level is achievable experimentally, but the number of lines and their potential overlap increases as d^{*3}. Since powder lines have a finite width, clear resolution exists only at the lower θ values; at higher values of θ, they merge into semi-continuous profiles of mainly unresolved

Table 12.4 Some results of an indexing with CRYSFIRE

I_{20}	M_{20}	V (Å^3)	a (Å)	b (Å)	c (Å)	α (°)	β (°)	γ (°)	Link
20	22.3	562.15	7.746	11.482	6.321	90.00	90.00	90.00	*ITO*12
20	21.2	280.53	5.000	11.475	4.991	90.00	101.6	90.00	*KOHL*
20	12.6	560.97	9.982	11.475	5.000	90.00	101.6	90.00	*KOHL*
20	12.1	562.15	7.746	11.481	6.321	90.00	90.00	90.00	*ITO*12
20	9.0	561.64	9.995	11.505	4.986	90.00	104.3	90.00	*TREOR*90
20	6.5	1966.5	16.737	11.507	10.210	90.00	90.00	90.00	*DICVOL*91
20	6.0	623.25	13.048	4.894	11.090	90.00	118.3	90.00	*TREOR*90
19	24.5	561.56	7.742	11.473	5.001	90.00	90.00	90.00	*KOHL*
19	8.0	561.90	9.973	11.508	5.001	90.00	101.8	90.00	*TREOR*90

maxima, each of which may contain 5–50 peaks. As long as the average discrepancy between the observed and calculated Q values is less than about 5%, the true unit cell can be extracted from among other approximate solutions.

A wholly exhaustive search is prohibitive. We have shown in Sect. 2.2.2 that a lattice can be described by any number of alternative unit cells, recognized by having the same reduced unit cell and volume. Less satisfactory solutions will usually occur, but they may be recognized through goodness-of-fit parameters, such as M_{20}, defined by (12.10); the higher the values of these parameters, the better is the fit.

The program system CRYSFIRE is actually a master automatic-indexing script, which operates through another program CRYS acting as a front-end "wizard" to a collection of eight indexing programs written by other workers of lengthy experience in the field of powder indexing, each having its own strategy and its own best applicability. The CRYSFIRE system has succeeded in indexing numerous powder patterns of all symmetries [27, 28].

As an example of indexing with CRYSFIRE, a set of 40 Q values for a particular powder sample was input to the program. A series of possible solutions were obtained, listed in Table 12.4 in order of number of lines I_{20} listed out of the first 20, together with the figure of merit M_{20}, the unit-cell volume and other parameters, and the particular link of the program that produced the solution. The program also recorded other possible solutions with I_{20} less than 19. All solutions are indicated as either orthorhombic or monoclinic.

The first solution listed in Table 12.4, with the highest figure of merit and with I_{20} equal to 20, reproduced all 40 observed Q values, although the experimental error in some lines was greater than the best achievable. This result may be regarded as the most probable, and a good starting point for further investigations. From a perusal of the indices found by the program, the following limiting conditions were deduced:

$$
\begin{aligned}
hkl : h + k = 2n \quad & 0kl : (k = 2n) \quad h0l : (h = 2n) \\
& hk0 : (h + k = 2n) \\
& h00 : (h = 2n) \quad 0k0 : (k = 2n) \\
& 00l : \text{None}
\end{aligned}
$$

Hence, we may conclude that the best solution is, $a = 6.321$ Å, $b = 7.746$ Å, and $c = 11.482$ Å, reordered so that $c > b > a$, with the possible space group being one of *Cmmm*, *Cmm*2, and *C*222. However, at this stage we have not considered the problem of overlapping lines, and it may be

necessary to review the deduction of the space group after the powder pattern has been decomposed into integrated intensities.

We consider briefly some of the remaining solutions in Table 12.4. The second solution indicates a smaller unit-cell volume, with an apparently monoclinic unit cell. It can be explained by the transformation (from solution 1) $\mathbf{a}' = \mathbf{a}/2 + \mathbf{b}/2$, $\mathbf{b}' = \mathbf{b}$, $\mathbf{c}' = -\mathbf{a}/2 + \mathbf{c}/2$, to give a P unit cell, but it would not be chosen as the conventional cell. The penultimate solution in Table 12.4, with $M_{20} = 24.5$, is almost as satisfactory, and would probably make a suitable starting point in the absence of solution 1. Several other solutions also involve an interaxial angle greater than 90°. The only other apparently different *orthorhombic* unit cell listed in Table 12.4 has a volume of 1966.5 Å^3, where the transformation (from cell 1) $\mathbf{a}' = 2\mathbf{a} + \mathbf{c}$ leads to the value 16.732 Å, and $|\mathbf{a} + \mathbf{c}|$ is approximately 10.0 Å. Thus, we have a set of unit cells within one and the same lattice, and we have chosen the most probable and conventional one.

We note in passing that the CRYSFIRE suite is a very powerful indexing system. However, because of the demise of the author in 2005, this suite is no longer under development, but is available from CCP14. We discuss indexing systems with built-in structure solving and refinement in Sect. 12.8.2.

12.6 Extracting Integrated Intensities from a Powder Pattern

At this stage, it is always prudent to check whether or no the pattern now indexed has already been recorded and to what extent the structure has been determined, by reference to the ICDD [3] records, to which we referred in Sect. 12.1. If we find a "new" pattern, we proceed to obtain the intensity data.

The extraction of individual intensities from a powder pattern is complicated by the overlapping of reflections in the pattern. Overlaps may be exact, as imposed by symmetry, or accidental, arising from near-equivalence of d values for nonequivalent reflections. Pattern decomposition is usually carried out either by the Le Bail procedure, which is based on the Rietveld method for determining F_o, or by the Pawley procedure, which is a least-squares approach with constraints.

12.7 The Rietveld Procedure

It is clear from Fig. 12.3 that the circle of which A_1A_2 is an arc is one of a set arising in reciprocal space from a very large number of randomly oriented crystallites in the sample. The intensity of each such diffraction record depends on the crystal structure, overlaps of reflections, and the physical and structural features of the diffraction procedure itself that we have discussed above.

The Rietveld refinement [29, 30] is a complex curve fitting problem. The model parameters, atomic coordinates, and thermal parameters and occupancies are subjected to a least-squares procedure so as to obtain the best fit between the whole experimental powder diffraction profile and the corresponding pattern calculated from the trial structure. In this way, the explicit decomposition of overlapping reflections can be avoided, because only the points along the observed and calculated profiles, and not the individual reflections, are compared.

A powder diffractometer record consists of a number of peaks, some overlapped, over a smooth background; the intensities follow a Poisson distribution which, with sufficient counts at each measurement step, is very closely Gaussian. The powder pattern is, thus, digitized into i steps to give an intensity function y_i; the digitizing parameter is either the scattering angle 2θ for X-rays or a velocity function in the case of TOF neutron studies. At each step i, there is an observed profile intensity $y_{o,i}$ and a background $y_{b,i}$. A corresponding calculated profile intensity $y_{c,i}$ is a mathematical

expression for the ith step comprising the adjustable parameters of the model: x, y, z coordinates, temperature factors, population parameters, and geometrical factors of the experiment. Hence, $y_{c,i}$ may be written in the form

$$y_{c,i} = y_b + \sum y_{\mathbf{h}} \tag{12.11}$$

where y_b is a background intensity and the summation term ($\mathbf{h} = hkl$) includes the Bragg reflections around the powder pattern step. When the number of observations, the profile measuring points, exceeds the number of parameters, a least-squares minimization M becomes appropriate for fitting a function to the observed data:

$$M = \sum w(y_o - y_c)^2 \tag{12.12}$$

The weight for any term is calculated from the variance in the corresponding measurement of y_o, and the calculated profile is given by

$$y_c = K|F_{\mathbf{h}}|^2 \Phi(P_{\mathbf{h}}) \tag{12.13}$$

where K is a constant that includes the scale and other experimental factors and $\Phi(P_{\mathbf{h}})$ is a profile function. Equation (12.13) represents a multidimensional surface with many minima. The minimum is found from

$$\sum w(y_o - y_c)\frac{\partial y_c}{\partial p_i} = 0 \tag{12.14}$$

p_i being the ith adjustable parameter.

Several different forms have been used for the profile function Φ: one of the simplest, which is appropriate for constant wavelength neutron data, is the Gaussian

$$\sqrt{\frac{C}{\pi H_j^2}} \exp\left[-C\frac{(2\theta_i - 2\theta_j)^2}{H_j^2}\right] \tag{12.15}$$

where C is 4 ln 2 and H_j is the full width of the peak at half-maximum height of the jth Bragg reflection. The pseudo-Voigt distribution, which is a combination of a Gaussian and a Lorentzian, is used frequently to model the peak shape in X-ray diffraction patterns [31]; the Gaussian is of the form noted above, while the Lorentzian may be expressed as

$$\frac{2}{\pi H_j}\left[1 + 4\frac{(2\theta_i - 2\theta_j)^2}{H_j^2}\right]^{-1} \tag{12.16}$$

The best fit of the calculated pattern to the observed pattern is judged by means of numerical criteria. Some of the criteria functions used are

$$R_F = \frac{\sum_j \left|\sqrt{I_{obs,j}} - \sqrt{I_{calc,j}}\right|}{\sum_j \sqrt{I_{obs,j}}} \tag{12.17}$$

which is the conventional R-factor, but written in terms of $\sqrt{I}$ instead of |F|;

$$R_{\mathrm{B}} = \frac{\sum_j |I_{\mathrm{obs},j} - I_{\mathrm{calc},j}|}{\sum_j I_{\mathrm{obs},j}} \tag{12.18}$$

which is called the Bragg R-factor;

$$R_{\mathrm{p}} = \frac{\sum_j |y_{\mathrm{obs},j} - y_{\mathrm{calc},j}|}{\sum_j y_{\mathrm{obs},j}} \tag{12.19}$$

which is the profile R-factor; and

$$R_{\mathrm{wp}} = \sqrt{\frac{\sum_j w_j (y_{\mathrm{obs},j} - y_{\mathrm{calc},j})^2}{\sum_j w_j (y_{\mathrm{obs},j})^2}} \tag{12.20}$$

which is the weighted profile R-factor: w_j is a weighting factor for the jth point. A goodness-of-fit indicator χ^2 is also used, given by

$$\chi^2 = (R_{\mathrm{wp}}/R_{\mathrm{e}})^2 \tag{12.21}$$

where R_{e} is the statistically expected R-factor:

$$R_{\mathrm{e}} = \frac{N - P + C}{\sum_j w_j (y_{\mathrm{obs},j})^2} \tag{12.22}$$

Here, N is the number of observations j in the experimental powder profile, P is the number of parameters refined, and C is the number of constraints. In general, N is much greater than $(P + C)$ so that the numerator tends closely to N. We shall indicate values for these parameters in the next section. Probably the most meaningful parameter is R_{wp}, since the numerator is the residual in (12.12) that is minimized. However, it is sensitive to a small number of poor agreements, which could arise from impurity.

The Rietveld method, now used generally for powder studies, was programmed first by Rietveld [26], but it is now available in many program packages. The system RIETAN (see Appendix D), which is a system similar to GSAS, offers additionally a choice of three minimization algorithms that can be introduced under user-control in one and the same minimization process.

A problem with Rietveld refinement, as with other forms of minimization, is the possibility of converging into a false minimum. The risk can be ameliorated by making reasonable variations to the starting model and refining, hopefully, to the same minimum. The three algorithms provided in RIETAN also provide for a possible way out of false minima. Guidelines for structure refinement using the Rietveld method have been published by the International Union of Crystallography (IUCr) Commission on Powder Diffraction [32].

12.7.1 The Le Bail Method

In this procedure, Le Bail et al. extended a method used by Rietveld [29, 33] to extract intensities for the calculation of Fourier maps during the course of a whole-profile refinement to the case where no initial structural model is available.

In the Rietveld procedure, the profile is defined by a number j of digitized points and, in the case of a resolved peak, the background-subtracted points are summed. For overlapping peaks 1 and 2, the integrated intensities J_{obs} are obtained through the equations

$$J_{1_{\text{obs}}} = \sum_j \frac{I_{1,\text{calc}} q_{1,j}}{I_{1,\text{calc}} q_{1,j} + I_{2,\text{calc}} q_{2,j}} (P_j - B_j) \tag{12.23}$$

$$J_{2_{\text{obs}}} = \sum_j \frac{I_{2,\text{calc}} q_{2,j}}{I_{1,\text{calc}} q_{1,j} + I_{2,\text{calc}} q_{2,j}} (P_j - B_j) \tag{12.24}$$

where $J_{1,\text{obs}}$ is equal to $m_1 F^2_{\text{o},1}$; m_1 is the multiplicity factor for $F_{\text{o},1}$, $I_{1,\text{calc}}$ is the calculated value of $F^2_{\text{o},1}$ based on an appropriate model, and $q_{1,j}$ contains the Lorentz, polarization, absorption (if necessary), and shape factors associated with peak 1, and similarly for peak 2, $(P_j - B_j)$ is the measured (peak − background) term for the jth point in the pattern. By summing (12.23) and (12.24) we obtain

$$J_{1,\text{obs}} + J_{2,\text{obs}} = \sum_j (P_j - B_j) \tag{12.25}$$

so that the sum of the peak areas is equal to the background-subtracted area, as in the case of resolved peaks.

The Le Bail procedure itself [34] is essentially an iterative version of that of Rietveld, Sect. 12.7, to evaluate |F|, in which the observed peak area for the nth iteration is used as the calculated peak area for the $(n + 1)$th iteration; generally, a rapid convergence is obtained for overlapping reflections. The procedure is programmed and available in systems such as FULLPROF and GSAS (Appendix D). It is said that the Le Bail method has led to a marked and radical increase in the ability to solve structures from powder diffraction data.

12.7.2 The Pawley Method

An alternative procedure for determining peak intensities in the absence of a structural model has been given by Pawley [35]. Whereas the Rietveld procedure is a least-squares analysis of a diffraction pattern where the principal variable parameters are peak position, peak shape, and those parameters dependent on peak area (atomic coordinates, thermal parameters, and intensity correction factors), the Pawley method is a least-squares analysis of the powder pattern in which the variable parameters are again peak position and shape but those concerning the peak area are the peak area itself. No structural model is needed, and the method is available in the program system ALLHKL [35, 36]. In both the Le Bail and Pawley algorithms, the variables that are related to peak positions and shapes are the same as in the Rietveld structure refinement method.

12.8 Examples of Solved Structures

Once the intensity data are available, attempts can be made to solve the phase problem, so as to obtain a structural model that can be subjected to at least a partial refinement. The attack may take place by means of the so-called traditional approach, that is, by Patterson or direct methods along the lines

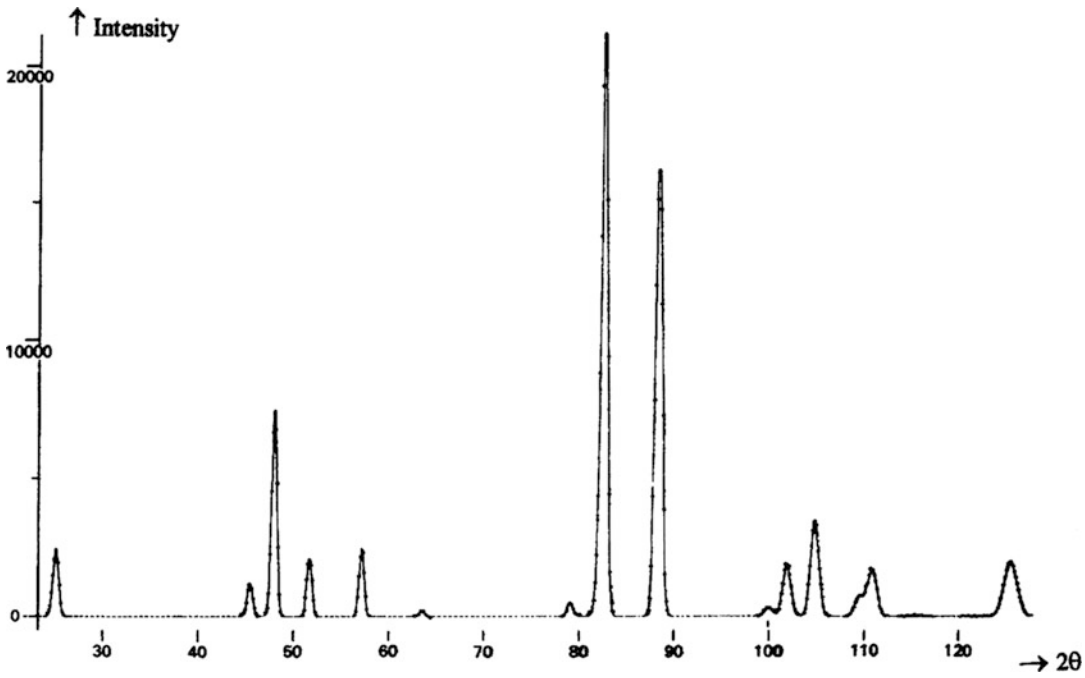

Fig. 12.11 Neutron diffraction pattern of a powdered sample of $CaUO_4$, measured at $\lambda = 2.565$ Å; the full line shows the calculated profile and the dots indicate the observed profile

discussed for single crystals, or newer techniques such as Monte Carlo, simulated annealing, and maximum entropy can be brought to bear on the problem. As with single-crystal structure determination, Patterson methods tend to be applied where heavy atoms are present in the molecules, and a direct method is used mainly for equal-atom structures. Refinement usually involves a combination of difference-Fourier syntheses to locate any missing atoms and Rietveld whole-profile structure refinement. We shall examine some structures with a view to indicating the stages that have been found necessary in obtaining satisfactory solutions.

12.8.1 Traditional Methods

Calcium Uranate

The early work by Rietveld was carried out with data obtained by neutron diffraction, but the use of X-rays, and particularly with a synchrotron source, is now well developed. Figure 12.11 shows an early diffractogram obtained by neutron diffraction on calcium uranate, $CaUO_4$. The fitted and experimental profiles show excellent agreement [37].

Manganese Phosphate Monohydrate

This structure, originally thought to be a $1\frac{1}{2}H_2O$ hydrate, was solved by Patterson methods [38], using X-ray powder diffractometer data collected at a synchrotron source. X-rays of wavelength 1.3208 Å were selected by means of a Ge (111) monochromator, and the radiation scattered in the vertical plane was measured.

The pattern was indexed by the program ITO, and the unit cell at an M_{20} of 196 had the dimensions $a = 6.916$ Å, $b = 7.475$ Å, $c = 7.361$ Å, and $\beta = 112.32°$; Z was 4, and the space group either Cc or

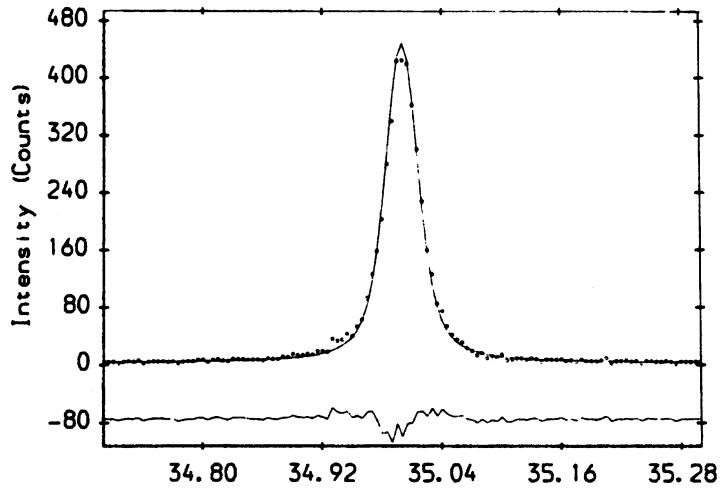

Fig. 12.12 Manganese phosphate monohydrate, $MnPO_4 \cdot H_2O$, modeled profile: plot of the intensity of the observed (dots) and calculated (solid line) profiles as a function of 2θ for the $31\bar{1}$ peak. The lower difference curve shows the accuracy of the pseudo-Voigt modeling function

$C2/c$ from systematic absences. We may note here that it may be inadvisable to decide the presence or absence of a center of symmetry solely by statistical tests, as the distribution of F_o values can be affected by the methods of pattern decomposition [39, 40]; space group $C2/c$ was confirmed by the structure analysis.

Pattern decomposition was carried out with the pseudo-Voigt function, leading to 61 intensity data; Fig. 12.12 shows a typical modeled peak. The intensity data were used to generate a Patterson map. The manganese atom coordinates were determined from this map and a difference-Fourier synthesis located the phosphorus and three oxygen atoms.

Refinement was carried out by minimizing the function $\sum_j w_j(y_{\text{obs},j} - Cy_{\text{calc},j})^2$, where the terms have the meanings already discussed, and C is a scaling constant. The weights for each jth point were calculated from the expression $w_j = [(y_j + b_j)] = \sigma^2(b_j)]^{-1}$, where b_j is the background at the jth point and $\sigma(b_j)$ is the esd of b_j. During refinement it was determined that the substance was, in fact, a monohydrate. Satisfactory final refinement was achieved, with the following agreement factors:

$$R_B = 4.74\%, \quad R_p = 12.2\%, \quad R_{wp} = 16.1\%, \quad R_e = 15.4\%, \quad \chi^2 = 1.1$$

Cimetidine

The structure of cimetidine, $C_{10}H_{16}N_6S$, has been solved from powder diffraction data [41]. In this example, a diffractometer and a synchrotron source of wavelength 1.4599(1) Å were used to obtain the data. The diffractogram was indexed by the program TREOR ($M_{20} = 176$) and the pattern decomposed by a modified Pawley method. Several attempts were made with direct methods programs, which located only sulfur and three other atoms. Further phase extraction was carried out with the direct methods program SIR88 (see below).

The structure was completed by iterative Fourier and least-squares procedures. A difference-Fourier synthesis then located all hydrogen atoms. After final Rietveld refinement, the structure converged with the following residuals:

$$R_B = 1.9\%, \quad R_{wp} = 8.5\%, \quad R_e = 6.9\%, \quad \chi^2 = 1.5$$

It is noteworthy that in the absence of the hydrogen atoms R_B and R_{wp} were 11.3% and 16.2%, respectively. Figure 12.13 illustrates the profile refinement of cimetidine with and without the inclusion of the hydrogen atoms.

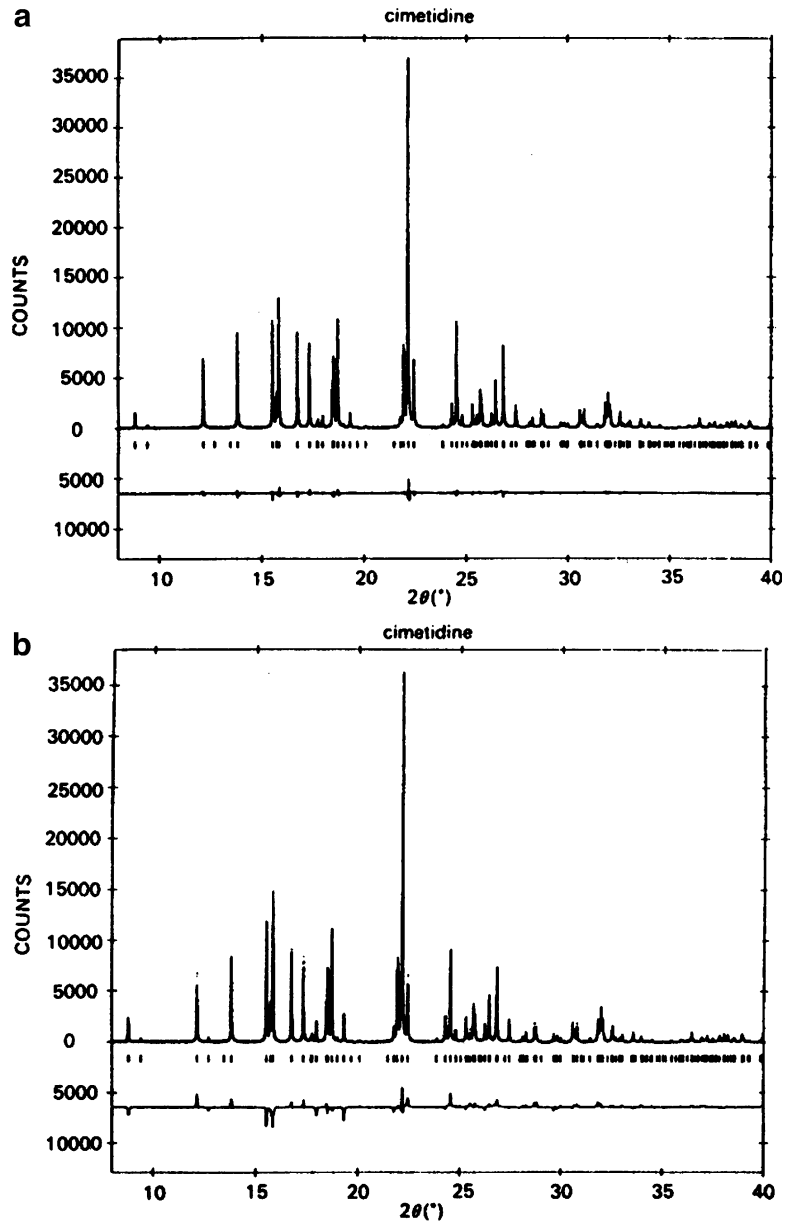

Fig. 12.13 Rietveld profile refinement of cimetidine. (**a**) With hydrogen atoms included, $R_{wp} = 8.5$ %. (**b**) Without hydrogen atoms included, $R_{wp} = 16.2$ % (after Cernik loc. cit.)

12.8.2 SIR Program System

In the context of direct methods here, SIR, as in SIR2004 [36], refers to phase determination by the method of *seminvariants representations* and should not be confused with SIR as used in Chaps. 7 and 10 wherein it means *single isomorphous replacement*.

A structure seminvariant is a linear combination of phases, the value of which is uniquely determined by the crystal structure alone, irrespective of the choice of permissible origin. For example, in space group $P2_1$ (y axis unique), $\phi(h0l)$ is a seminvariant if h and l are both even. Again, if $h_1 + h_2 + h_3 = 2n$, $k_1 + k_2 + k_3 = 0$, and $l_1 + l_2 + l_3 = 2n'$, where both n and n' are integers, then $\phi(\mathbf{h}_1) + \phi(\mathbf{h}_2) + \phi(\mathbf{h}_3)$ is

a seminvariant. Further discussions of the properties of structure seminvariants may be found in the literature [42].

The SIR method is based on the estimation of 1- and 2-phase structure seminvariants and 3- and 4-phase structure invariants, according to the theory of representations [43, 44]. The program functions in all space groups without user intervention, although a knowledge of partial structure moieties may be exploited with advantage. A later version of SIR, SIR2008, has been published [45, 46] (see also Appendix D).

Silver–Pyrazole Complex

The structure of the silver–pyrazole complex $[Ag(pz)]_3$ (pz = pyrazole), $C_9H_9N_6Ag_6$, has been solved by direct methods [47] as part of a program investigating complexes between pyrazole, $C_3H_4N_2$, and copper or silver.

Powder diffractometer data were collected with graphite-monochromatized X-radiation of wavelength 1.5418 Å, at values of 17–85° in 2θ-steps of 0.02°. The program TREOR was used to index the pattern, and it gave the orthorhombic unit cell $a = 13.13$ Å, $b = 10.56$ Å, and $c = 8.79$ Å with $M_{20} = 15$. The indexed data suggested the space group *Pbcn*, which was confirmed by the structure analysis. The refined unit cell had the dimensions $a = 13.1469(4)$, $b = 10.5702(10)$, and $c = 8.7921(4)$. Since $Z = 4$, there are 12 Ag(pz) moieties in the unit cell.

Pattern decomposition was achieved by the Pawley method through application of the program ALLHKL to 924 reflection data, using 3400 points. The program SIRPOW92 (see below) was used to extract a direct methods trial model comprising the three silver atoms in the asymmetric unit, one of which lies on a twofold axis. At this stage, $R_p = 0.29$ and $R_{wp} = 0.37$. The structure was completed and Rietveld refinement, excluding hydrogen atoms, converged with the following set of indicating parameters:

$$R_F = 6.0\%, \quad R_p = 11.5\%, \quad R_{wp} = 14.9\%,$$
$$R_e = 6.6\%, \quad \chi^2 = 5.1$$

The value of χ^2 is larger than normal for a refined structure. It has been noted [48] that the parameters R_e and χ^2 depend on the intensity counting statistics and are, at best, only gross goodness-of-fit parameters.

12.8.3 EXPO Program System

The program SIRPOW92 that was employed in the structure determination just described has been incorporated into the powerful structure-solving program system EXPO that is now much used. The main addition to the SIRPOW92 system is the routine EXTRA, the purpose of which is to provide for the decomposition of the pattern according to the Le Bail algorithm. Figure 12.14 illustrates the flow diagram for EXPO. Advances in pattern decomposition have made it possible to introduce into EXTRA the positivity of the electron density and Patterson functions, the treatment of pseudo-translational symmetry and preferred orientation, and the availability of a partial structure. Such information, when detected in SIRPOW, is recycled as shown in Fig. 12.14, so as to obtain better extracted values for F_o^2. Additional user-friendly facilities include contouring of Fourier maps, representation of crystal structures by coordination polyhedra, and automatic preliminary Rietveld refinement, which is triggered when the structure is incomplete. A more recent innovation is the labeling of peaks in electron density maps, based on chemical information rather than on electron density peak heights [36].

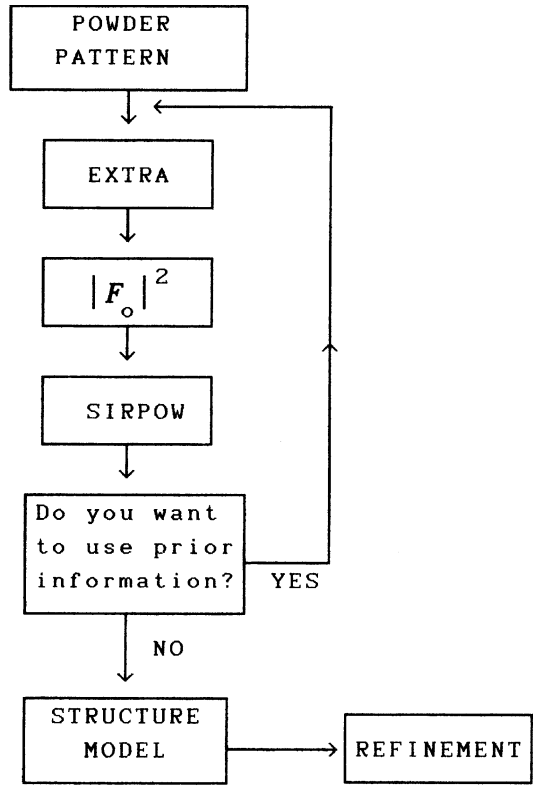

Fig. 12.14 Flow diagram for the program system EXPO; structural information detected by SIRPOW can be recycled to EXTRA, so as to obtain more reliable intensity data (after Altomare et al., loc. cit. [49])

The EXPO system has been made available to the academic community by the courtesy of its authors, and can be obtained from a web site (see Appendix D); several versions have been described in the literature [49, 50], the latest version [51] being EXPO2009.

12.9 Direct-Space Methods

Direct-space methods, not to be confused with traditional direct methods, have evolved from model building techniques in which chemical information is used in order to construct a sensible structural model. Such a model can then be used as a basis for calculating a diffraction pattern with which to compare the measured pattern. The inclusion of information on bond lengths, bond angles, connectivities, torsion angles, orientation, and position means that a very large number of chemically sensible models could be produced. Thus, computing power must be brought to bear in order for such an approach to be practicable. Encoding frequently results in algorithms being specific to a given class of compounds.

In the case of molecular compounds, information on bond lengths and bond angles is well documented, so that the number of variables is reduced to that defining orientation and position, and possibly torsion. In the case of zeolite structures, for example, the chemical composition and connectivities of structural units are of significance in designing useful structural models.

An alternative approach involves generating a model by the random placement of atoms of the required number and types in the unit cell, then applying shifts to the atoms in predetermined amounts, and calculating and comparing patterns so as to find a best fit. Constraints in terms of known chemical information can be introduced into the model, so as to increase the plausibility of the model and to reduce the time consumption of computing facilities. We consider examples of these and other related techniques in the remainder of this section.

12.9.1 Zeolites and the FOCUS Algorithm

Zeolite structures have many important applications as molecular sieves, absorbents, catalysts, and ion-exchange materials. These properties are related to both their unusual structures and, in particular, to their framework topologies, that is, the way in which the tetrahedral structural units are linked in the solid state. As zeolites are microcrystalline, powder diffraction proves to be the only method available for their detailed structural examination.

The structures are complex, often with high symmetry, such as $P\frac{6_3}{m}mc$ or $Fm\bar{3}c$, and can have unit cells, with dimensions up to 40 Å, so that a high degree of overlap of diffraction maxima arises. Generally, direct methods have been used for solving the structures, with difference-Fourier synthesis and Rietveld profile refinement to complete and refine the structure [16].

A different approach is used in the program environment FOCUS [52], indicated in Fig. 12.15, where Fourier recycling is combined with a specialized topology search and topology classification scheme. The method makes use of crystal-chemical information such as chemical composition, probable interatomic distances, and the fact that all zeolite structures have three-dimensional four-connected frameworks, in order to aid in the interpretation of electron density maps.

The Q values of about 20 high-accuracy powder lines serve to determine the unit-cell parameters and index the pattern. The space group follows from the indexed lines, and integrated intensities are extracted.

Random phases consistent with the space group are assigned to the extracted reflection intensities and an electron density map generated. If enough of the phases are (by chance) correct, some of the features of the structure will appear, and an attempt is made to interpret the map using the chemical information outlined above. The resulting model is then used to generate new phases and a new electron density map. This Fourier interpretation and recycling procedure is continued until either phase convergence or a maximum number of cycles is reached. Then the process is started again, if necessary, with a new set of random phases. Each time an electron density map is generated, a search is also made for a three-dimensional four-connected net.

If one is found, it is classified and written to a file. The procedure is terminated when a sufficient number of such nets have been found. The net that occurs most frequently is usually the correct framework structure. The model is then used as a starting point for structure completion and Rietveld refinement. Figure 12.16 illustrates the FOCUS algorithm, the detail of that section of Fig. 12.15 that is enclosed by dashed lines.

12.9.2 Zinc–Silicate Complex VIP-9

As an example of a large structure solved only when the FOCUS procedure was applied, we cite the zinc-silicate molecular sieve complex [54] VPI-95. The synthesized material corresponds in chemical composition to $Rb_{38–43}K_{5–10}[Si_{96}Zn_{24}O_{240}]\cdot 48H_2O$, from chemical analysis and ^{29}Si NMR spectroscopy. Room temperature powder patterns were collected on a Scintag XDS 2000 powder

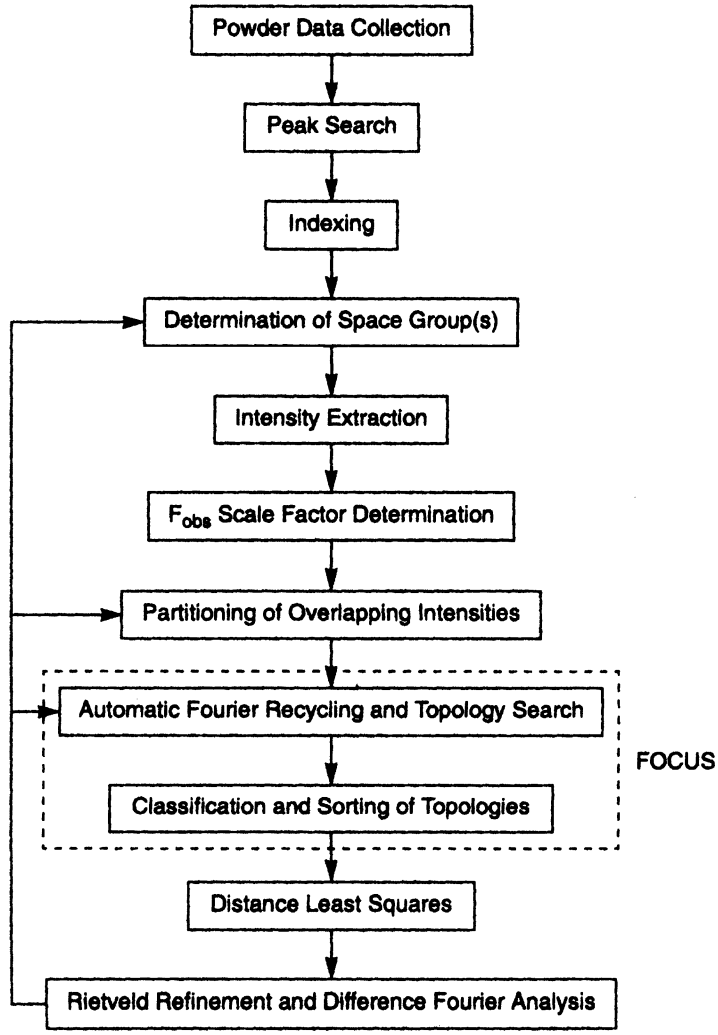

Fig. 12.15 The FOCUS structure-solving environment, tailored to the solving of zeolite structures. The essential algorithm for the zeolites is enclosed in dashed lines; the remaining blocks in the diagram refer to standard procedures [53]

diffractometer, operating in Bragg-Brentano geometry, with a flat-plate sample and Cu $K\alpha$ radiation ($\lambda = 1.54184$ Å). Most of the peaks were indexed on a hexagonal unit cell, with $a \approx 9.9$ Å and $c \approx 37$ Å.

A sample exchanged with $(NH_4)^+$ was used, in addition to the as-synthesized sample, in order to obtain high-resolution powder patterns at the European Synchrotron Radiation Facility (ESRF) at Grenoble. The pattern of the $(NH_4)^+$-exchanged sample was indexed completely in space group $P\frac{4_2}{n}cm$, with $a = 9.8946$ Å and $c = 36.8715$ Å. The framework topology was determined by applying the FOCUS procedure, as described above. While a preliminary Rietveld refinement indicated that the topology was probably correct, this model was not pursued because the exchange was incomplete and the detection of $(NH_4)^+$ in the presence of H_2O would be difficult.

The pattern of the as-synthesized material was indexed only in space group $P4_12_12$, with $a = 9.8837(1)$ Å and $c = 73.6505(6)$ Å, an approximate doubling along c compared to the $(NH_4)^+$-exchanged compound. Rietveld refinement was applied with restraints on the (Si, Zn)–O bond length, and the O–(Si, Zn)–O and (Si, Zn)–O–(Si, Zn) bond angles. A series of difference-Fourier

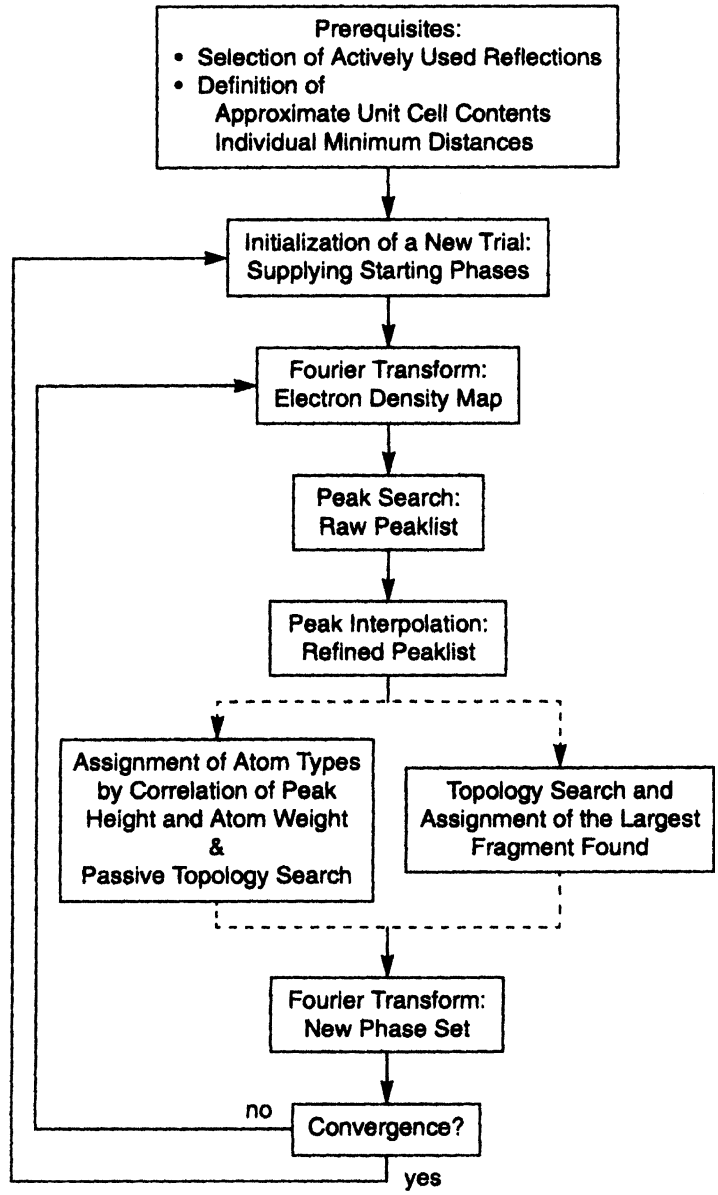

Fig. 12.16 The FOCUS algorithm in detail (compare Fig. 11.14): automatic Fourier recycling and topology searching is carried out here (after Grosse-Kuntsleve, loc. cit. [53])

maps based on iteratively improved models led to better agreement, but only as far as $R_F = 0.167$ and $R_{wp} = 0.453$.

By applying further chemical reasoning to the model, together with a new series of difference-Fourier maps and Rietveld refinement, gradual improvements in the model were obtained. The final refinement converged at $R_F = 0.069, R_{wp} = 0.147, R_e = 0.099$, and $\chi^2 = 2.2$. In all, 170 structural parameters were refined, which is one of the largest framework topology structures solved from powder data without manual intervention. Figure 12.17 shows profiles for the Rietveld refinement of the as-synthesized VIP-10.

The framework topology has seven T-sites, or nodes [51, 55] in the asymmetric unit. The framework can be described in terms of two types of layers linked by isolated tetrahedra,

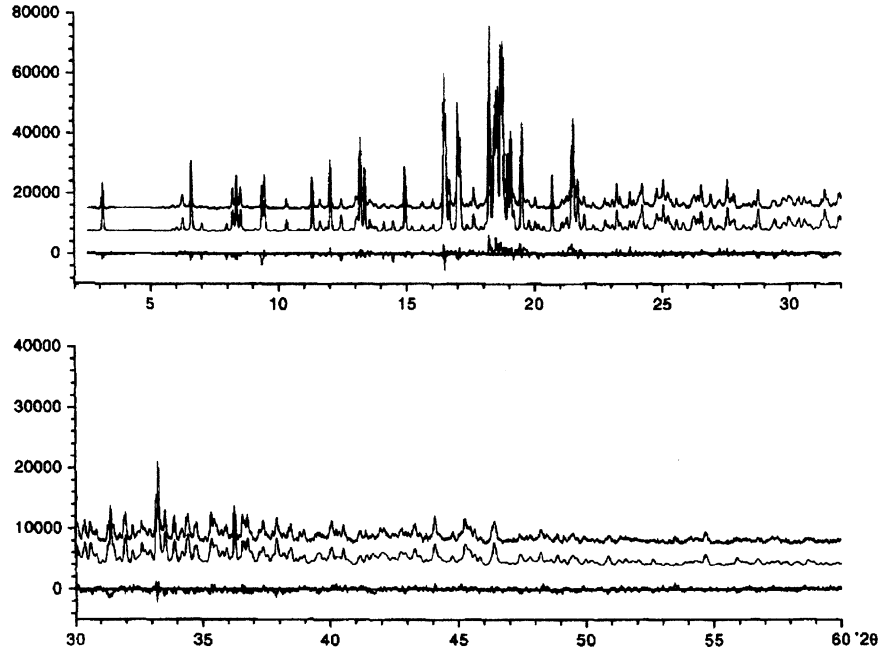

Fig. 12.17 Profile refinement for VIP-9, 0–30° (*top*) and 30–60° (*bottom*) in 2θ. In each diagram, the top, middle and bottom profiles refer to the observed, calculated, and difference patterns, respectively

Figs. 12.18 and 12.19. The simpler layer A is a 4.8^2 net, which is a two-dimensional string of undulating 4-membered rings (4-rings) and 8-rings, as shown in Fig. 12.18.

The building unit of layers B is a polyhedron consisting of a 3-ring with three bent 5-rings attached to it, which may be termed a $[5^3 3]$ structural unit. The polyhedra share 3-ring faces on one side, and 5-ring edges on the other side, thus forming infinite chains parallel to $\langle 110 \rangle$. Neighboring, parallel chains are shifted relative to one another by a half-chain length, and these structural units are new to zeolite data.

12.10 Monte Carlo Method

In this approach, a series of structural models in direct space is generated by random movements of a set of atoms in the unit cell, and each state of the system is evaluated on the basis of the agreement between the observed and calculated powder diffraction patterns. The models are postulated independently of the diffraction data, and once a satisfactory model has been obtained, it is refined by the Rietveld procedure. The atom positions may be chosen independently at random, as a group of atoms known to be part of the structure, particularly if the group forms a rigid body, or in terms of the connectivity of a molecule. In the latter case, the molecule is usually described in terms of internal coordinates, that is, bond lengths, bond angles, and torsion angles, that are converted into Cartesian coordinates, and the variables are the orientation and positions of the molecule in the unit cell. In some cases, unknown torsion angles may be additional variables.

The Monte Carlo method itself is based on the well-known Metropolis algorithm [56], and each state of the system is tested by calculating a residual R_{wp}, rather than an energy term as in its original applications. An initial configuration of atoms $\mathbf{x}_i$ is displaced in a random manner but with

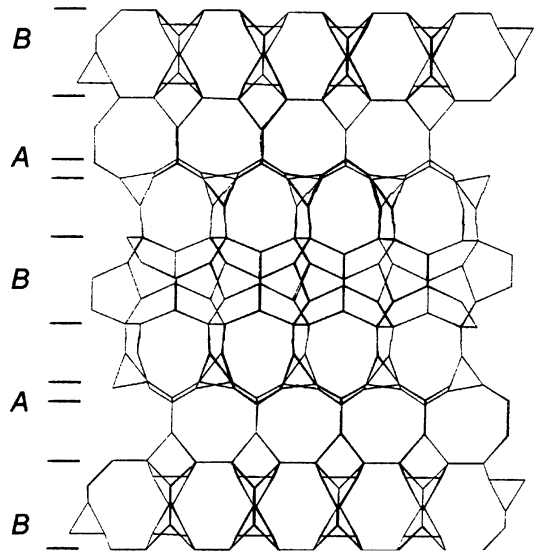

Fig. 12.18 The framework topology of VIP-9 viewed along [110]; oxygen atoms have been omitted for clarity. Layer B at $z = \frac{1}{2}$ is rotated by 90° with respect to those at $z = 0$ and 1. Similarly layer A at $z = \frac{3}{4}$ is rotated by 90° relative to that at $z = \frac{1}{4}$

constraints, relating, for example, to the amount of change permitted in the parameters of the set $\mathbf{x}_i$, which may involve translations (in x, y, z), rotations about orthogonal axes (in θ, ϕ, Ψ) and torsion movements (in τ_1, τ_2, τ_3, ...).

After each movement, the powder pattern is calculated, scaled to the observed pattern, and the whole-profile R_{wp} factor calculated. Alternatively, the extracted intensities can be used as long as an account is taken of the correlations between neighboring reflections [57].

Each trial structure is assessed on the basis of the difference Z, such that

$$Z = R_{wp}(\mathbf{x}_{current}) - R_{wp}(\mathbf{x}_{previous}) \tag{12.26}$$

($Z \leq 0$), $\mathbf{x}_{current}$ is accepted; if $Z > 0$, $\mathbf{x}_{current}$ is accepted with a probability $\exp(-Z/S)$, where S is a scaling factor that operates like the energy parameter kT in the more conventional applications of the Metropolis algorithm [58]. It follows that the probability for rejection is $[1 - \exp(-Z/S)]$: if $\mathbf{x}_{current}$ is rejected, the previous trial structure now becomes "current." These stages are repeated, Fig. 12.20, so generating a Markov chain, that is, a sequence of events in which the outcome of each step is independent of the previous step; the probability of the change $\mathbf{x}_i \rightarrow \mathbf{x}_j$ depends only on the states i and j. Eventually, the event showing the lowest R_{wp} value is subjected to Rietveld refinement. This technique has now been applied successfully to a number of structures [11, 59]. An important feature of the Metropolis algorithm is that it biases the generation of configurations towards those that are significant for the true solution.

p-Bromophenylethanoic Acid

An interesting application of the Monte Carlo method elucidated the previously unknown structure of *p*-bromophenylethanoic acid, $BrC_6H_4CH_2CO_2H$ [60]. By computer indexing of the first 20 lines of the powder pattern, the unit-cell dimension found were $a = 16.020$ Å, $b = 4.607$ Å, $c = 11.715$ Å, and $\beta = 109.33°$. The systematic absences indicated space group $P2_1/c$, with $Z = 4$.

The Monte Carlo technique was applied in two stages. In stage 1, the bromine atom alone was used. Of 1000 moves, one was found to be the most probable, at $R_{wp} = 5.2\%$; the value of R_{wp} for a

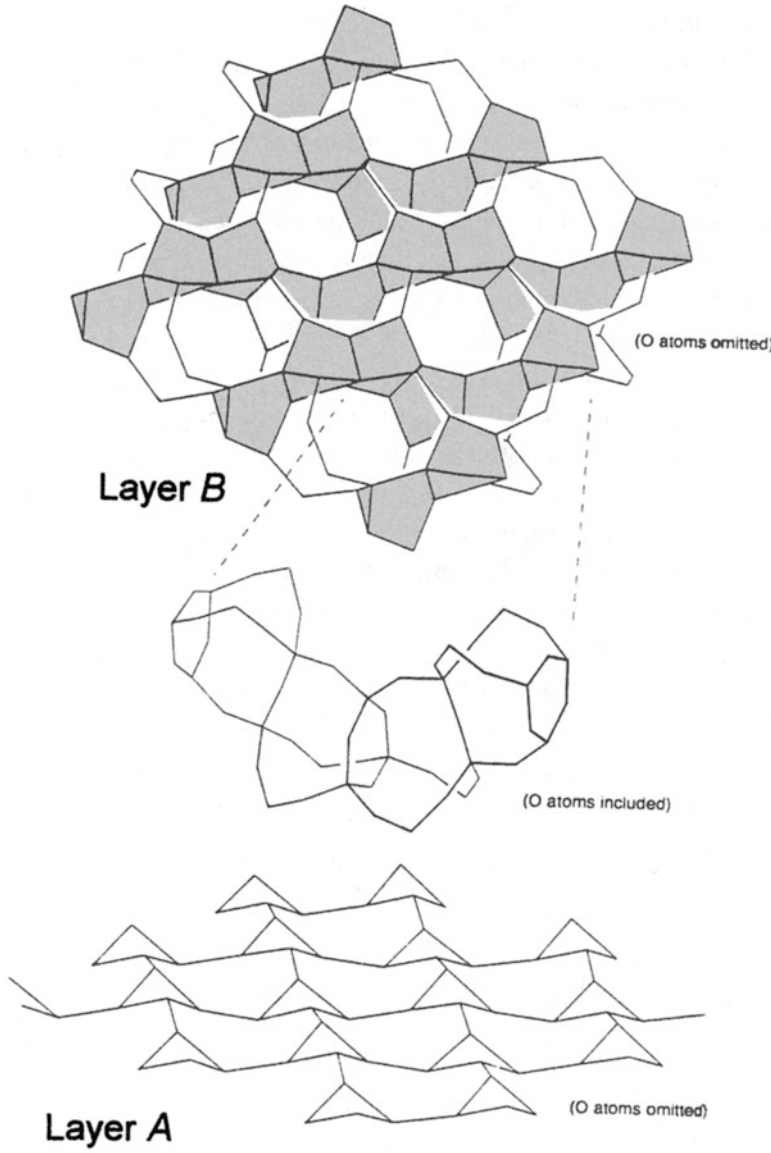

Fig. 12.19 Layer-like building units in VIP-9: layer *A*, 4.8^2 net; layer *B*, chains of $[5^3 3]$ polyhedra

totally random placement is ca. 55%. In the second stage, the bromine atom was constrained in its best determined position, and the rigid C_7 fragment of the molecule rotated at random about an axis passing through the bromine atom. From the best fit model from this stage, the remaining atoms were obtained by difference-Fourier methods, and Rietveld refinement of the structure converged at $R_{wp} = 6.66\%$.

Figure 12.21 illustrates the powder diffraction profiles from the Rietveld refinement. The difference between the stage 1 and final bromine atom positions was 0.2 Å, and other differences up to 1.3 Å were recorded for other atoms. This analysis shows well the power of this technique, which may now be considered one of the standard methods in the crystallographer's armory.

Another structure that has been solved successfully by the Monte Carlo method is that of 5-bromonicotinic acid [61].

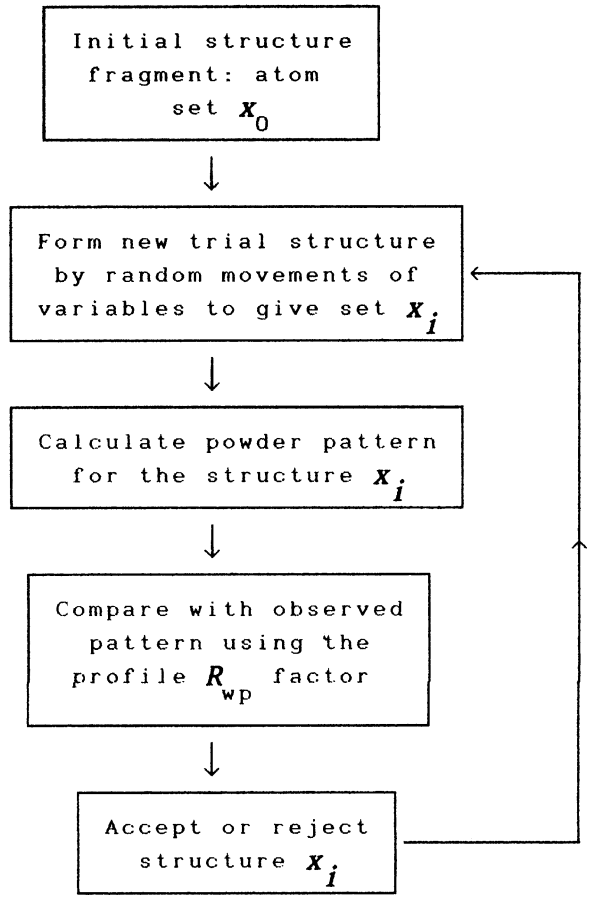

Fig. 12.20 Monte Carlo cycling procedure. If a trial structure $\mathbf{x}_i$ is accepted, it becomes $\mathbf{x}_{i+1}$ and is cycled back; otherwise $\mathbf{x}_i$ is returned for new random movements

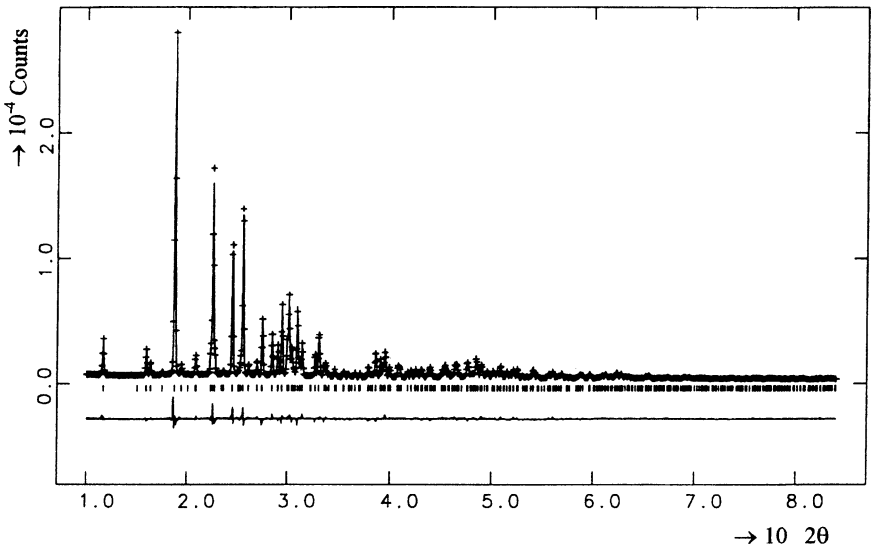

Fig. 12.21 Profile refinement for *p*-$BrC_6H_4CH_2CO_2H$; the experimental points are marked + and the calculated profile is the full line. The lower line is the difference-Fourier profile

12.10.1 Simulated Annealing

The simulated annealing procedure [62] can be combined with the Monte Carlo method. In this case, the Metropolis algorithm is applied as before but with a systematic decreasing of the parameter S in the exponential function above, which is similar to a decrease in temperature of the energy quantity kT. The temperature controls the potential energy surface that is scanned, and the Metropolis loop accepts the lower energy solution. A higher energy solution can be accepted if the temperature is raised. The starting value of S is set such that all trial structures are accepted; then, as S is decreased, so the poorer fits (larger R_p values) are excluded. The final structure, the best fit, is then subjected to Rietveld refinement. In cases where the model does not contain the whole structure, the remainder can usually be located by difference-Fourier synthesis, Sect. 8.4.5.

Variations in this procedure have been proposed differing in the selection of the S parameter [63] and the rate at which it is changed or in the generation of trial configurations. One such variant has been incorporated into the program system DASH [65].

12.11 ESPOIR Program System

While Monte Carlo methods imply an element of random-sampling, the fitting of a model to scattering data in this context is sometimes termed a reverse Monte Carlo procedure. The program system ESPOIR [35, 66] employs the reverse Monte Carlo technique coupled with simulated annealing for ab initio structure determination. It can use a completely random starting model, or else incorporates a structural entity of known geometry, in which case it functions similar to molecular replacement.

The program fits the starting model to either F_o data extracted from a powder pattern, or to single-crystal data in the unlikely event that one of the single-crystal techniques fails. The author of the ESPOIR program system has kindly consented to its inclusion with the suite of programs supplied with this book.

An innovative and important computer-time-saving feature of this program relates to the problem of overlapping peaks. Direct-space methods generally either fit the raw data to a model and derive measures of fit for each model, or fit some equation involving the extracted F_o data, taking into account overlapping of peaks. ESPOIR follows a method intermediate between these two: instead of fitting the raw data, a pseudo powder pattern $P(2\theta)$ is reconstructed from the extracted F_o data. In this way no background, Lorentz, polarization, absorption, asymmetry, profile shape, or reflection multiplicity corrections have to be considered. A Gaussian shape function G is used for fast calculation and gross approximation to the overlapping, and the best fit between the pseudo pattern and the calculated pattern may be judged from the parameter R_{wp}, where

$$R_{wp} = \frac{\sum |P(2\theta)_{obs} - KP(2\theta)_{calc}|}{\sum P(2\theta)_{obs}} \tag{12.27}$$

where $P(2\theta)_{obs} = GF_o$ and K is a scale factor. Simulated annealing is introduced so as to reduce progressively the magnitude of the atomic displacements. An additional variable parameter permits the acceptance of Monte Carlo events that do not necessarily decrease R_{wp}, so as to avoid false minima; about 40% of such events are retained typically. Nevertheless, at least ten independent runs are recommended for a chance of success. With a more complex structural problem, more runs may be needed.

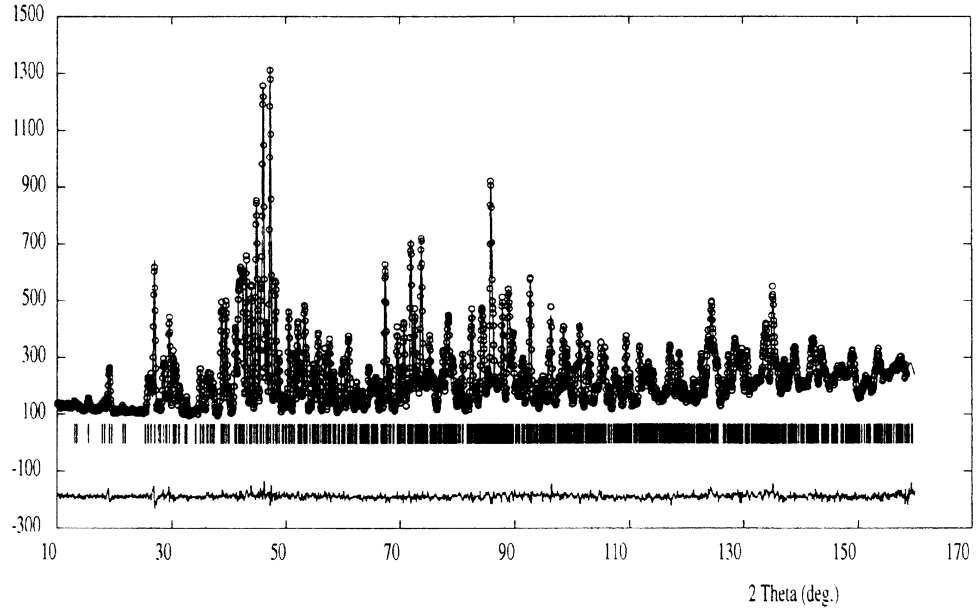

Fig. 12.22 Final profile refinement for α-$La_2W_2O_9$: circles, observed pattern; full line, calculated pattern; vertical lines, reflection positions; bottom profile, difference pattern

The ESPOIR procedure is illustrated with examples and problems at the end of Sect. 13.8ff. It must be borne in mind that ESPOIR is a program for obtaining a starting model for further refinement, either by the Rietveld technique or by traditional procedures. As with all other procedures, ESPOIR is not guaranteed to lead to success: (Fr. *espoir* = hope).

α-Lanthanum Tungstate

α-Lanthanum tungstate, $La_2W_2O_9$, crystallizes in space group $P\bar{1}$, with $a = 7.2489(1)$ Å, $b = 7.2878(1)$ Å, $c = 7.0435(1)$ Å, $\alpha = 96.367(1)°$, $\beta = 94.715(1)°$, $\gamma = 70.286(1)°$, and $Z = 2$. Diffraction patterns were obtained with both X-rays (Cu $K\alpha$) and neutrons ($\lambda = 1.5939$ Å). The pattern was indexed by TREOR to give a single triclinic solution ($M_{20} = 24$). Using the X-ray data, intensities were extracted by the program FULLPROF and the structure solved by SHELXS-86 to locate two lanthanum and two tungsten sites. No full solution was found at this stage: the scattering from oxygen in the presence of lanthanum and tungsten is relatively weak.

The structure was solved with the neutron data using the program ESPOIR [67]. A $[WO_4]$ tetrahedron was first used as a rigid-body search fragment, rotating around fixed positions for tungsten and lanthanum. However, R_p would reduce no lower than 25%. Finally, the lanthanum and tungsten positions were fixed at the coordinates given by the X-ray study, and nine oxygen atoms searched with ESPOIR by a random approach, using the neutron data. An R_p of 6.2% was achieved, and then the whole neutron pattern subjected to a final Rietveld refinement. Figure 12.22 illustrates the final profile refinement, and Table 12.5 summarizes results from the X-ray and neutron studies.

The differences between the two tabulated sets of results probably relate to preferred orientation, which was considered to be the cause of the failure to find the oxygen atoms by difference-Fourier synthesis, thus leading to the poorer agreement indices. One aspect of the structure is shown in projection in Fig. 12.23. The tungsten atoms are of two types: W1 is coordinated by five oxygen atoms forming a trigonal bipyramid, whereas W2 is coordinated octahedrally. This structure could explain the failure of the models based on $[WO_4]$ tetrahedral units. The sharing of corners builds up

Table 12.5 Results from the X-ray and neutron data collection for α-$La_2W_2O_9$

	X-ray	Neutron
Number of reflections	1317	1366
Number of parameters refined	58	69
Peak-shape function	Pseudo-Voigt	Pseudo-Voigt
R_B	0.114	0.030
R_p	0.156	0.060
R_{wp}	0.186	0.069
R_e	0.064	0.019

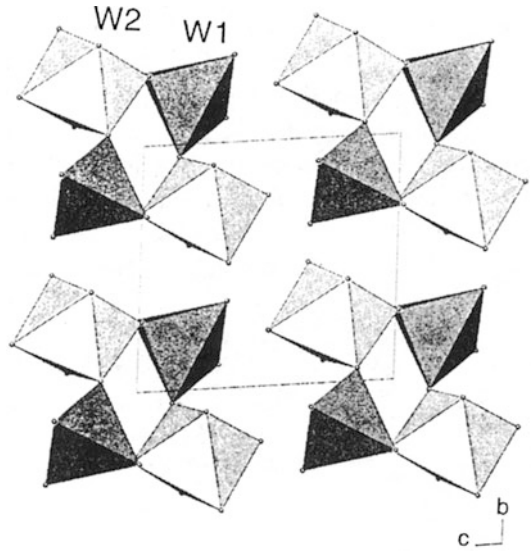

Fig. 12.23 Projection of the structure of α-$La_2W_2O_9$ along *a*, showing the two environments of the tungsten atoms

4-rings to give $[W_4O_{18}]$ structural units in a *cyclo*-tungstate structure. The two lanthanum atoms are coordinated, respectively, by nine and ten oxygen atoms.

12.12 Powder Diffraction with Proteins

X-ray diffraction analysis of the structure of a protein is often limited by the availability of suitable single crystals. However, it has been shown that the absence of single crystals may not present an insurmountable difficulty in this field any more than it does in materials science, as powder diffraction techniques have developed to the point where, as we have seen in the previous section, complex oxides, zeolites, and small organic molecular structures are often solved from powder data alone.

12.12.1 T3R3 Zinc–Insulin Complex

The applicability of powder diffraction methods to proteins has been demonstrated, for example, with the structure solution and refinement of a new variant of the T3R3 human zinc–insulin complex [68], produced by mechanically grinding a polycrystalline sample.

High-resolution synchrotron X-ray powder-diffraction data were used to solve this crystal structure by molecular replacement adapted for Rietveld refinement. A complete Rietveld refinement of the 1630-atom protein structure, achieved by combining 7981 stereochemical restraints with a 4800-step ($d_{min} = 3.24$ Å) powder-diffraction pattern, yielded the residuals $R_{wp} = 3.73\%$, $R_p = 2.84\%$, and $R_F = 8.25\%$.

It was found that the grinding-induced phase change was accompanied by 9.5 and 17.2° rotations of the two T3R3 moieties in the crystal structure. The material reverts in 2–3 days to give the original T3R3 crystal structure. A Rietveld refinement of this 815-atom protein structure, by combining 3886 stereochemical restraints with a 6000-step ($d_{min} = 3.06$ Å) powder-diffraction pattern, yielded the residuals $R_{wp} = 3.46\%$, $R_p = 2.64\%$, and $R_F = 7.10\%$.

The ability, demonstrated by this work, to solve and refine a protein crystal structure from powder diffraction data indicates that this approach could be employed, for example, to examine structural changes in a series of protein derivatives in which the structure of one member is known from a single-crystal study. An interesting paper on the application of powder methods to proteins has been given in the literature [69].

12.13 Maximum Entropy in Crystal Structure Analysis

12.13.1 Most Probable Distribution

Entropy is a thermodynamic concept that may be used to describe the degree of order in a system. Although it was defined originally in terms of the operation of heat engines, it can also be addressed in terms of the probability of a system at a molecular level.

Initially, imagine L gaseous electrons behaving ideally, where L is the Avogadro number, constrained to one-half V_1 of a total containing volume V_2 and then allowed to expand reversibly at constant temperature so as to occupy the total volume V_2. The probability that any given electron is now present in the volume V_1 is $\frac{1}{2}$. The probability that two such electrons are present in V_1 and the probability that the two electrons are in the volume V_1 would be $(\frac{1}{2})^2$, since these two events are uncorrelated. Thus, the probability that all L electrons occupy the volume V_1 is $(\frac{1}{2})^L$, and W_1/W_2 is, therefore, $(\frac{1}{2})^L$, where W_1 is less than W_2. Since any similar ratio of volumes could be chosen, $W_1/W_2 = (V_1/V_2)^L$. From the study of heat engines, we know that the heat change q_{rev} in the expansion of a gas behaving ideally from a volume V_1 to a volume V_2 is given by $q_{rev} = nRT \ln(V_2/V_1)$ per mole, where n is the amount of substance and R is the universal gas constant. But q_{rev}/T is a measure of the molar entropy change ΔS, so that $\Delta S = R \ln(V_2/V_1)$. In our analysis, $n = 1$ and the volume that of the electron gas;

$$\begin{aligned}\Delta S = S_2 - S_1 = R \ln(V_2/V_1) = R(\ln W_2 - \ln W_1]^{1/L} = (R/L)[\ln W_2 - \ln W_1] \\ = k_B[\ln W_2 - \ln W_1]\end{aligned} \tag{12.28}$$

where k_B is the Boltzmann constant. Thus the entropy of a system is identified with probability through the Boltzmann equation:

$$S = k_B \ln W \tag{12.29}$$

Table 12.6 Numbers W of arrangements of five electrons among five boxes B0–B4

B4	B3	B2	B1	*B*0	W
1	1	1	1	1	5!/1! = 120
2		1		2)	
2			2	1)	
1	2			2)	5!(2!2!)
1		2	2	)	30 each = 180
	2	2		1)	
	2	1	2	)	
1		3		1)	
1	1		3	)	5!/5! = 80
	3		1	1)	20 each
	1	3	1		
		5			1

We can look upon the probability W as the number of ways a system can be constructed within a fixed framework. Consider distributing five identical but distinguishable electrons among a set of boxes B0–B4 such that the total number of boxes is 10. The possible arrangements are set out in Table 12.6.

Of the 381 possible arrangements, one distribution is four times more probable than the next most probable distribution. As the number of electrons increases, one distribution becomes outstandingly more probable: this is the maximum entropy distribution and is assumed to be the true distribution.

12.13.2 Electron Density Map

Consider the grid points at which an electron density map is normally calculated. The number of electrons available for these sites is given and the unit cell defines the boundaries for the electron distribution. If the electrons were distributed at random, a map could be produced but it would be unlikely to be correct. The number of ways in which the electrons can be arranged to form a map is a measure of the probability that we need to determine.

The problem is similar to that described for the distribution of electrons in boxes, but instead of electrons in boxes we have electrons in cells corresponding to the grid points at which an electron density map is calculated. We consider a total of N electrons in a unit cell divided into M grid points. The first electron has a choice of N cells in which to go: a mutually exclusive assignment has a probability $p_i = n_i/N$, where p_i is the probability of the ith electron assignment and n_i the number of electrons assigned in that choice. If the total number of electrons is large, the probability of any particular result is the multinomial distribution familiar in Maxwell-Boltzmann-statistics: $P(\mathbf{p}) = W/M^N$, where W is given by

$$W = \frac{N!}{n_1!n_2!n_3!\ldots n_m!} \tag{12.30}$$

The most probable result is that which maximizes the value of W, the total number of arrangements of the N electrons among the M cells. We write

$$\frac{1}{N}\ln\ W = \frac{1}{N}\ln\left(\frac{N!}{n_1!n_2!\ldots n_M}\right) = \frac{1}{N}\ln\left(\frac{N!}{Np_1!Np_2!\ldots Np_M}\right) = \frac{1}{N}\left(\ln\ N! - \sum_{i=1}^{M}\ln\ Np_i!\right) \quad (12.31)$$

Applying Stirling's approximation for factorials:

$$\begin{aligned}\frac{1}{N}\ln\ W &= \frac{1}{N}\left(N\ln N - \sum_{i=1}^{M} Np_i \ln Np_i\right) = \ln N - \sum_{i-1}^{M} p_i \ln Np_i \\ &= \ln N - \ln N\sum_{i=1}^{M} p_i - \sum_{i=1}^{M} p_i \ln p_i = \left(1 - \sum_{i=1}^{M} p_i\right)\ln N - \sum_{i=1}^{M} p_i \ln p_i \\ &= -\sum_{i=1}^{M} p_i \ln p_i \end{aligned} \quad (12.32)$$

We showed in Sect. 12.13.1 that entropy is proportional to ln W, so that

$$S \propto -\sum_{i=1}^{M} p_i \ln p_i \quad (12.33)$$

Replacing p_i by the more usual symbol for electron density, we write

$$S \propto -\sum_{i=1}^{M} \rho_i \ln(\rho_i / r_i) \quad (12.34)$$

where ρ_i is the electron density in the ith grid cell and r_i is a reference density. The maximum value of S gives the most probable electron density distribution. Desirably [70], the reference density can incorporate constraints, such as the total number of electrons in the unit cell or reflections with known phase, or it may be taken as $\sum_i \rho_i$. The maximum entropy method has been discussed in the literature [71, 72] and used successfully to solve structures [70]. The method has been programmed successfully in BayMEM [73, 74], which can be used for crystallographic applications of the maximum entropy method. It can derive the electron density in the unit cell from phased X-ray diffraction data. Different types of Bayesian prior probable densities are available.

12.14 Log-Likelihood Gain in the Phase Problem

In 1984, Bricogne, and Bricogne and co-workers published approaches to the solution of the phase problem that involved a combination of multi-solution, maximum entropy, and likelihood ranking techniques [75–79].

12.14.1 Basis Set and Expansion of Reflections

We start with the preliminary data and the extraction of intensities, as already discussed. The extracted intensities can be divided into an "overlapped" set and a "non-overlapped" set. For example, in the

Table 12.7 LLG data for $Li_6Zr_2O_7$

Node	Entropy	LLG (non-overlap)	LLG (all data)
135	−2.03	7.10	15.1
109	−1.75	5.93	12.8
99	−1.87	4.89	11.3
97	−2.90	7.51	12.5

structure determination of Mg_3BN_3 [80], only about 3% of the intensity was overlapped, whereas with 1,3,4,6-tetrathiopentalene-2,5-dione [81], $C_4O_2S_4$, about 60% of reflections were overlapped.

An origin is set by assigning appropriate phases to a number of reflections, preferably of large |E| values, according to the rules already discussed; these n reflections constitute the starting, or basis, set {B}. The determination of |E| values requires the use of a Wilson plot or a K-curve procedure, Sects. 4.2.1 and 8.2.1. The basis set is used as constraints in constructing a maximum entropy map $\mu(\mathbf{x})$ [82], where maximum entropy has been discussed in Sect. 12.13ff. The Fourier transform of $\mu(\mathbf{x})$ reproduces the set {B} and also estimates structure amplitudes and phases for m non-basis set reflections, {N}.

Reflections from {N} are added to {B} with appropriate phases: 0 or π for centric reflections and $\pm\pi/4$, $\pm$ $3\pi/4$ for acentric reflections, Sect. 8.2.9. Each phase combination creates a *node*: n_c centric reflections create 2^{n_c} nodes and acentric phases create 4^{n_a} nodes. The nodes develop a phase tree in which the root node is the origin-fixing reflection set from which subsequent levels are built by phase permutations.

12.14.2 Log-Likelihood Gain

Following Bricogne [83], a log-likelihood gain (LLG) expression is formulated as

$$\mathrm{LLG} = \mathrm{LH} - \mathrm{LH}_0 \tag{12.35}$$

where LH is the LLG function, namely, the probability that a given overlap of a set of $E_{\mathbf{h},0}$ values and the corresponding $|E_{\mathbf{h},c}|$ from maximum entropy calculations, and LH_0 represents the null hypothesis, that is, with zero number of calculated intensities. Table 12.7 shows some results from an LLG calculation. The inclusion of overlapped reflections generally leads to the best result. With four second-level node phases for the structure of lithium zirconium diphosphate [9], $Li_6Zr_2O_7$, space group $C2/c$, there are 148 non-overlapped and 109 overlapped reflections. Node 135 generated a correct electron density map. Here, entropy is a poor figure of merit but LLG, including overlaps, indicates the correct solution well.

12.14.3 Centroid Maps

In maximum entropy calculations, centroid electron density maps [84], including overlapped reflections, are most useful. These maps employ experimentally determined |E| values with phases from the relevant tree node for the basis set reflections, whereas non-basis set reflections incorporate |E| amplitudes generated from the |F| data set and phases generated from a maximum entropy process and with Sim-type weighting.

12.15 Genetic Algorithms

Another optimization technique, apart from Monte Carlo and simulated annealing, is based on genetic algorithms [85, 86] which make use of the evolutionary strategy of Darwinian theory.

The procedure follows a series of steps [87]:

1. An individual random starting population, normally of a given size, is generated, and may be likened to a *chromosome*. The components are a collection of variables of the crystal structure, the *genes* x_j, $(j = 1, 2, \ldots n)$.
2. The individual is characterized by its *fitness*, that is, the degree to which its calculated diffraction pattern agrees with the experimentally observed pattern.
3. Then, by applying the genetic operators of *crossover* and *mutation*, new and improved structures are produced from a population and subjected to fitness tests.

   In a crossover, or mating, the chromosomes of two individuals, or parents, are cut, either singly or at multiple points, and the cut parts interchanged:

	Parent 1	Parent 2
Initial state	*ABCDEF*	*GHIJKL*
Crossover state	*ABCJKL*	*GHIDEF*

   Mutation can be carried out by assigning a new random value to one or more of the x_i genes, or by inverting a variable through the origin.
4. *Natural selection* is applied in the form of a fitness test: by the principle of the "survival of the fittest," the population evolves towards a correct, or substantially correct structure, suitable for further refinement.

The processes 1–4 represent one generation; further generation are executed by cycling back until a global minimum is found. In common with least-squares refinement and other minimization procedures, a local minimum may be encountered leading to a *stagnation* in the population. The way out is always the fitness test based on a comparison of F_o and $|F_c|$. The genetic algorithm technique has been programmed and has solved crystal structures successfully [88].

12.16 Energy Minimization Techniques

We have described a method of structure analysis by energy minimization in the context of single crystal studies in Sect. 9.11.3. It has been shown that a similar process can be successful with data obtained by powder methods [89]. The procedure with powder data can be summarized in the following stages:

- The experimental powder pattern is indexed and, where possible, the space group deduced
- A plausible structure is devised based on standard molecular geometry, with constraints dependent upon symmetry and upon packing parameters, such as the unit-cell dimensions, and positional and orientational disposition of the molecule within the asymmetric unit
- Possible crystal structures are calculated by minimization of the lattice energy of the postulated structure model, and powder patterns are calculated for the possible structures
- The better solutions are selected by comparison with the experimental powder pattern and then subjected to Rietveld refinement, so as to obtain a minimum lattice energy structure

12.17 Concluding Remarks

The examples of structure determination discussed in this chapter demonstrate the feasibility of solving crystal structures from powder diffraction data. It is to be expected that the methods will become even more widely used in future, since it opens the way for the investigation of a wide spectrum of materials that have previously resisted detailed structural analysis. At the present time, however, it remains that the resolution obtained from powder diffraction is not yet as good as that obtained from single crystal studies.

The totality of techniques has been well reviewed [90–92] (and Bibliography), and many programs and program systems have been devised that address both the individual stages and the complete process of solving crystal structures from powder data [32]. The serious powder analyst is strongly recommended to consult these literature sources. In addition, there are several important references relating to work that have not all been published elsewhere that can be accessed from web sites; they are listed in Table 12.8.

As an example of the results obtainable with state-of-the-art equipment, we illustrate the high-resolution powder diffraction pattern of (E)-1-cyclopropyl-6-fluoro-4-oxo-7-(4-(3-oxo-3-phenyl-prop-1-enyl)piperazin-1-yl)-1,4-dihydroquinoline-3-carboxylic acid, Fig. 12.24 (R = C_6H_5). It was taken at the Diamond Light Source synchrotron, which was discussed in Sect. 3.1.6, on beamline IO3 with a wavelength of 0.9763 Å over a period of 1 s, and recorded on a Dectris Pilatus 6M large area pixel detector. The photograph is shown in Fig. 12.25.

Table 12.8 Crystallographic data on web sites

Topic	Web site
Structure determination from Powder Diffractometry Round Robin (SDPDRR)	http://www.cristal.org/SDPDRR/index.html, http://www.ccp14.ac.uk/ccp/web-mirrors/armel/SDPDRR/index.html
Optimum data collection strategy	http://www.ccp14.ac.uk/solution/powder_data_collection.html, http://www.ccp.14.ac.uk/solution/gsas/convert_vct_data_to_gsas.html
Discussion on variable count time (VCT) data collection	http://www.ccp14.ac.uk/solution/vct/index.html

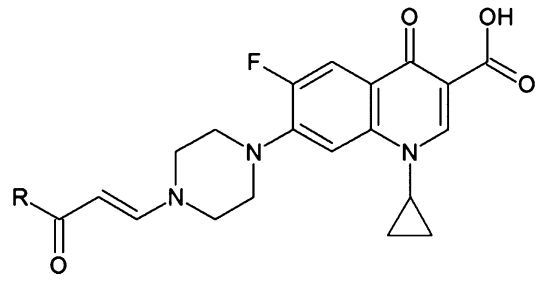

Fig. 12.24 The molecular structure of (E)-1-cyclopropyl-6-fluoro-4-oxo-7-(4-(3-oxo-3-phenylprop-1-enyl)piperazin-1-yl)-1,4-dihydroquinoline-3-carboxylic acid (R = C_6H_5)

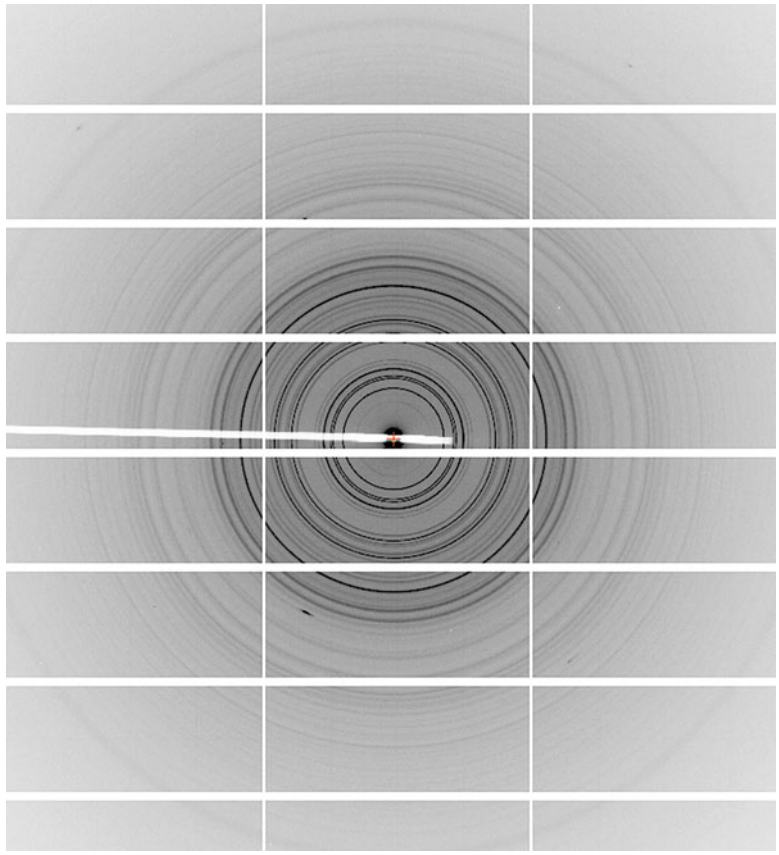

Fig. 12.25 The powder diffraction pattern of crystals of the compound in Fig. 12.24. The grid lines are a feature of the detector system, and do not influence the measurement of intensities (Sample supplied by Professor Ali El Dissouky (Alexandria University). Powder record by courtesy of J. Nicholson and E. Shotton, Diamond Light Source, UK.)

12.18 Problems

12.1. A cylindrical powder camera has a radius of 57.30 mm. A given powder specimen is examined with Cu $K\alpha$ radiation. At what value of the Bragg angle θ would the $\alpha_1\alpha_2$ doublet begin to be resolved on the film, if the lines in that region of the film are of approximately 0.5 mm thickness? The α_1 and α_2 components have wavelengths 1.5405 Å and 1.5443 Å, respectively, and an intensity ratio $\alpha_1{:}\alpha_2 = 2$.

12.2. The following sequence of $\sin^2\theta$ values was measured for lines on a powder photograph of a cubic substance taken with Cu $K\alpha$ radiation, $\lambda = 1.5148$ Å. Determine (a) the unit-cell type, (b) the indices of the lines, (c) a best value for the unit-cell dimension a. For (c), plot a, calculated for each line, against $f(\theta) = \frac{1}{2}(\cos^2\theta/\sin\theta + \cos^2\theta/\theta)$, with θ in radian, and extrapolate to $f(\theta) = 0$. This (Nelson–Riley) function tends to compensate for errors arising from absorption, specimen eccentricity, camera radius, and beam-divergence.

0.0465, 0.0635, 0.1717, 0.2486,
0.3712, 0.4170, 0.5394, 0.5544,
0.6609, 0.7368

12.3. Confirm the values of the parameters for the reduced unit cell of magnesium tungstate discussed in Sects. 12.3 and 12.3.1 with the program LEPAGE: use the default value of the collinearity parameter C, and also $C = 0.5°$.

12.4. The following unit-cell parameters were deduced from an indexed powder photograph: $a = 8.515$ Å, $b = 8.515$ Å, $c = 6.021$ Å, $\alpha = 135.0°$, $\beta = 69.3°$, $\gamma = 90.00°$. Determine the reduced and conventional unit cell, and list its parameters. What is the ratio of the volume of the conventional unit cell to that of the given unit cell?

12.5. The following values (10^4Q) were obtained for the first 40 lines on an accurate powder diffraction record of the microcrystalline single substance X. Deduce by induction a possible unit cell. Remember that the first three lines need not necessarily correspond with a^*, b^*, and c^*. Hence, index the lines on the basis of this unit cell. What can be said about the unit-cell type and space group for crystal X? Obtain the reduced and conventional unit cells, using the program LEPAGE. If the conventional unit cell is different from the unit cell first derived, transform the indices. What now are the conventional unit-cell type and the possible space group(s)?

Line number	10^4Q	Line number	10^4Q
1	83.1	21	892.4
2	810.1	22	916.0
3	172.2	23	962.3
4	2410.8	24	981.7
5	332.6	25	9910.1
6	356.1	26	1016.0
7	416.0	27	1105.0
8	421.5	28	11210.0
9	4310.3	29	1134.0
10	516.9	30	1248.0
11	5510.8	31	12410.0
12	642.9	32	1308.0
13	648.6	33	1330.0
14	683.3	34	1361.0
15	688.8	35	13610.0
16	732.1	36	1397.0
17	748.4	37	14110.0
18	801.5	38	1425.0
19	837.2	39	1444.0
20	884.5	40	1461.0

12.6. In this problem and the next two, sets of data are provided to demonstrate the power and applicability of computer indexing, using the program ITO12. The first data set has been included with the suite of computer programs, because it is vital to set up the data in the prescribed format. For those familiar with FORTRAN, the fields for numerical input are F10.5; see also Sect. 13.7 for comments on ITO12. Crystal *XL*1: data are provided as values of 10^4Q; Q values are sometimes defined as $10^4/d_{hkl}^2$. Use the program to determine the unit-cell parameters and as much information as possible about the space group.

361.0	459.4	475.8	701.7	717.5	968.9	1310.0	1312.0
1059.0	1088.0	1363.0	1411.0	1428.0	1444.0	1653.0	1724.0
1785.0	1838.0	1902.0	2039.0	2081.0	2145.0	2300.0	2332.0
2380.0	2451.0	2485.0	2639.0	2656.0	2675.0	2807.0	2871.0
996.0	3185.0	3212.0	3250.0	3265.0	3402.0	3507.0	3428.0

12.7. Crystal *XL2*: data are provided as values of $10^4\ Q$. Use the program to determine the unit-cell parameters and as much information as possible about the space group.

311.5	364.2	442.0	675.4	877.8	1,020.3	1,065.2	1,111.0
1,150.3	1,246.3	1,384.4	1,456.3	1,500.2	1,534.1	1,605.3	1,610.0
1,767.6	1,773.4	1,839.5	1,954.9	2,045.3	2,157.1	2,228.7	2,242.5
2,311.0	2,318.4	2,476.7	2,702.3	2,746.8	2,773.3	2,834.6	2,865.6
2,925.3	3,003.0	3,019.4	3,062.3	3,145.7	3,198.0	3,236.9	3,276.7

12.8. Crystal *XL3*: data are provided as values of 2θ. Use the program to determine the unit-cell parameters and as much information as possible about the space group.

8.44	15.45	15.61	16.19	17.00	17.22	18.32	18.80
19.02	20.71	22.20	22.29	23.98	24.92	25.14	25.76
26.95	27.34	28.01	29.10	29.27	30.70	31.18	31.62
32.04	32.49	32.83	33.30	33.60	34.67	34.87	35.45
36.63	36.84	37.11	37.34	38.08	38.57	38.89	38.95

Problems on *structure-solving* from power data are presented in Chapter 13, wherein ESPOIR is discussed further.

References

1. Hull AW (1917) Phys Rev 10:661
2. Debye P, Scherrer P (1816) Phys Zeit 17:277
3. http://www.icdd.com/education/xrd.htm
4. Williamson GK, Hall WH (1953) Acta Metall 1:22
5. Westgren A, Phragmén G (1928) Metallwirtschaft 7:700
6. Vegard L (1916) Phil Mag 32:187
7. Westgren A (1932) Angew Chem 45:33
8. Bibliography, Dinnebier RE (ed)
9. Bibliography, David WIF et al
10. Harris KDM et al (2001) Angew Chem Int Edit 40:1626
11. Harris KDM, Tremayne M (1996) Angew Chem Mater 8:2554
12. http://www.xhuber.com
13. Parrish W, Huang TC (1983) Adv X-ray Anal 26:35
14. Morris RE et al (1994) J Solid State Chem 111:52
15. Jeffrey GA et al (1987) Proc R Soc A 414:47
16. Bibliography, David et al
17. Bibliography, Young
18. http://pilatus.web.psi.ch/mythen.htm

19. http://www.dectris.ch/sites/mythen1k.html
20. Bergamaschi A (2010) J Synchrotron Radiat 17:653
21. Ito T (1949) Nature 164:755
22. Křivý I, Gruber B (1976) Acta Crystallogr A32:297
23. Niggli P (1928) Handbuch der Experimentalphysik, vol 7. Akademische Verlagsgesellschaft, Leipzig
24. Le Page Y (1982) J Appl Crystallogr B15:255
25. Spek AL (1988) J Appl Crystallogr 21:578
26. http://www.ccp14.ac.uk/tutorial/crys/program/ito12.htm
27. Shirley R (2002) Crysfire. http://www.ccp14.ac.uk
28. Shirley R (2002) Powder indexing with Crysfire. International Union of Crystallography Commission on Powder Diffraction, Newsletter, July 2002
29. Rietveld HM (1969) J Appl Crystallogr 2:65
30. Young RA (ed) (1993) The Rietveld method. Oxford University Press, Oxford
31. Young RA, Wiles DB (1982) J Appl Crystallogr 15:430
32. McCusker LB et al (1999) J Appl Crystallogr 32:36
33. Young RA (1993) The Rietveld method. Oxford University Press, Oxford
34. Le Bail A (1988) Mat Res Bull 23:447
35. Pawley GS (1981) J Appl Crystallogr 14:357
36. http://www.ccp14.ac.uk
37. Loopstra BO, Rietveld HM (1969) Acta Crystallogr 2:65
38. Lightfoot P et al (1987) Inorg Chem 26:3544
39. Cascarano G et al (1992) J Appl Crystallogr 25:310
40. Estermann MA et al (1992) J Appl Crystallogr 25:539
41. Cernik RJ et al (1991) J Appl Crystallogr 24:222
42. Ladd MFC, Palmer RA (eds) (1980), Theory and practice of direct methods. In: Crystallography. Plenum Press, New York, and references therein
43. Giacovazzo C (1977) Acta Crystallogr A33:933
44. idem. ibid. A36:362 (1980)
45. Burla MC et al (2003) J Appl Crystallogr 36:1103
46. http://www.nanomegass.com/files/eldiff.pdf
47. Masciocchi N et al (1994) J Am Chem Soc 116:7668
48. Hill RJ, Madsen IC (1987) Powder Diffr 2:146
49. Altomare A et al (2004) J Appl Crystallogr 37:1025; J Res Natl Stand Technol 109:125
50. Brunelli M et al (2007) J Appl Crystallogr 40:702
51. http://wwwba.ic.cnr.it/content/expo2009
52. Grosse-Kunstleve RW et al (1997) J Appl Crystallogr 30:985
53. Grosse-Kuntsleve RW (1996) PhD thesis, Dissertation ETH no. 11422, Zürich. http://cci.lbl.gov/~rwgk/Dissertation/
54. McCusker LB et al (1996) Micropor Mater 6:295
55. Grosse-Kuntsleve RW et al (1999) J Appl Crystallogr 32:536
56. Metropolis N et al (1957) J Chem Phys 21:1087
57. David WIF et al (2001) DASH user manual. CCD, Cambridge, UK
58. Allen MP, Tildesley DJ (1987) Computer simulation in liquids. Oxford University Press, Oxford
59. Tremayne M et al (1996) J Mater Chem 6:1601
60. Harris KDM et al (1994) J Am Chem Soc 116:3543
61. Harris KDM, Tremayne M (1996) Chem Med 8:2554
62. Engel GE et al (2001) Mol Cryst Liq Cryst 356:355
63. Andreev YG, Bruce PG (1998) J Chem Soc Dalton Trans 4071
64. David WIF et al (1998) Chem Commun 931
65. http://www.ccdc.cam.ac.uk/products/powder_diffrac tion/dash/
66. Le Bail A (2000) Seventh European powder diffraction conference, Barcelona. http://www.cristal.org/sdpd/espoir/
67. Laligant Y et al (2001) J Solid State Chem 159:223
68. von Dreele RB et al (2000) Acta Crystallogr D56:1549
69. Margiolaki I, Wright JP (2008) Acta Crystallogr A64:169
70. Bagautdinov B et al (1998) Acta Crystallogr B54:626
71. Gilmore C (1996) Acta Crystallogr A52:561
72. Sivia D, David W (1994) Acta Crystallogr A50:703
73. http://www.crystal.uni-bayreuth.de/en/baymem/index.html
74. van Smaalen S et al (2003) Acta Crystallogr A59:459

75. Bricogne G (1984) Acta Crystallogr A40:410
76. idem. ibid. A44:517 (1988)
77. Bricogne G et al (1992) J Mater Chem 2:1301
78. Bannister C et al (1989) Bayesian methods and maximum entropy. In: Skilling J (ed) Kluwer, Dordrecht
79. Gilmore CJ et al (1990) Acta Crystallogr A46:284
80. Hiraguchi H et al (1991) J Appl Crystallogr 24:286
81. Gilmore CJ et al (1993) Proc Math Phys Soc A442:97
82. Sakata M, Sato M (1990) Acta Crystallogr A46:263
83. http://erice2005.docking.org/vcourse/19thu/1145-Bri cogne/Bricogne.pdf
84. Gilmore CJ et al (1991) Acta Crystallogr A47:830
85. Kariuki BM et al (1999) J Chem Soc Chem Commun 1677
86. Shankland K et al (1998) Int J Pharmacol 165:117
87. Polak E (1971) Computational methods in optimization. Math Sci Eng 77
88. Johnston RJ et al (1997) The algorithm GAPSS. University of Birmingham, UK, and references therein
89. http://www.usc.es/export/sites/default/gl/investigacion/riaidt/raiosx/descargas/manuais/ and references therein
90. http://sdpd.univ-lemans.fr/egypt-2004/
91. http://www.cristal.org/rapport/LeBail_promo2004_ prod.pdf
92. http://lachlan.bluehaze.com.au/cpdnews98/art18.htm, and references therein
93. http://www.ccp14.ac.uk
94. Bragg WL (1949) The Crystalline State, Vol 1, Bell, London

Bibliography

David WIF, Shankland K, McCusker LB, Baerlocher C (eds) (2002) Structure determination from powder diffraction data. International Union of Crystallography, Oxford University Press, Oxford
Dinnebier RE, Billinge SJL (eds) (2008) Powder diffraction: theory and practice. RSC Publishing, Cambridge
Pecharsky VK, Zavalij PY (2005) Fundamentals of powder diffraction. Springer, Berlin
Peschar R (1990) Molecular structure solution. Procedures 3:59
Prince E (1985) In: Structure and statistics in crystallography. Wilson AJC (ed) Adenine Press
Schenk H (1982) In: Computational crystallography. Sayre D (ed) Oxford University Press, Oxford
Young RA (1993) The Rietveld method. International Union of Crystallography. Oxford University Press, Oxford